He II line intensity measurements in the JET tokamak

OPEN ACCESS
IOP Publishing
Plasma Physics and Controlled Fusion
Plasma Phys. Control. Fusion **66** (2024) 115001 (35pp)
https://doi.org/10.1088/1361-6587/ad75b9

He II line intensity measurements in the JET tokamak

K D Lawson[1,*], I H Coffey[1,2], M Groth[3], A G Meigs[1], S Menmuir[1], B Thomas[1] and JET Contributors[4]

[1] UKAEA, Culham Campus, Abingdon OX14 3DB, United Kingdom
[2] Astrophysics Research Centre, School of Mathematics and Physics, Queen's University Belfast, Belfast BT7 1NN, United Kingdom
[3] Aalto University, Otakaari 1, Espoo 02150, Finland

E-mail: Kerry.Lawson@ukaea.uk

Received 27 March 2024, revised 16 August 2024
Accepted for publication 30 August 2024
Published 16 September 2024

Abstract

An understanding of the behaviour of the D or He fuel used in tokamak discharges is essential in analyses such as modelling edge and divertor transport and the erosion of the vessel walls. However, poor agreement is found between measurements made on the JET tokamak and collisional-radiative models used to predict the hydrogen-like D and He line intensities. The range of temperatures of the plasmas emitting the radiation is also limited, in contrast to that for many impurities for which a wide range is possible. This is particularly so for He II whose line intensities tend to have the same near-constant ratios in most pulses, suggesting that the emission originates in plasma regions with very similar electron temperatures. To gain understanding and to allow quantitative comparisons with theoretical models, extensive observations of the VUV Lyman series have been made, for all discharge scenarios run during three He campaigns. Those for He discharges in both JET ITER-like wall (JET-ILW) and JET C (JET-C) campaigns are presented here. He discharges have the advantage of fewer impurities resulting in less complex spectra than when D is used as the fuel. However, the characteristics of the observed discrepancies are similar in both species, allowing He to be used as a proxy for D in order to gain understanding of the discrepancy. In addition, the study of He avoids the complication of molecular species contributing to the level populations. Opacity effects are also expected to be less severe in He discharges. Nevertheless, so as to ensure that the measurements are not unduly affected by opacity, comparisons have also been made with emission from Balmer and Paschen series members. Measurements of both line intensities and their ratios are presented for all-pulse surveys and for individual pulses. In exceptional cases in which the He emission is intense a dependence on the He II line intensity is demonstrated. The discrepancy between these measurements and the theoretical models is illustrated.

Keywords: JET, tokamak, He II line intensities, hydrogen-like collisional-radiative model, Lyman alpha discrepancy

[4] See Maggi et al 2024 (https://doi.org/10.1088/1741-4326/ad3e16) for JET Contributors.
[*] Author to whom any correspondence should be addressed.

1. Introduction

The behaviour and description of the D and He fuel in tokamak discharges impacts on a number of analyses important to the interpretation of the results from present day machines and predictions for future devices such ITER, DEMO and STEP. The Lyman α line of the hydrogen-like fuel species accounts for $\sim$90% of the power radiated by these species, this being an essential input to transport modelling of edge and divertor plasmas (Wiesen *et al* 2015, Bonnin *et al* 2016), necessary for describing the power exhaust (Tonello *et al* 2024) and the mechanisms controlling plasma detachment (Groth *et al* 2023, Verhaegh *et al* 2023). Collisional-radiative (CR) models form the basis of the description of the hydrogenic atoms used in investigating molecular interactions with the plasma (Verhaegh *et al* 2021). The modelling of the plasma surface interactions such as erosion and migration (Borodkina *et al* 2024, Romazanov *et al* 2024) also rely on a correct description and understanding of the behaviour of the fuel species. Yet, poor agreement is usually found between measurements on the JET machine and well established theoretical CR models used to predict the hydrogen-like line intensities of the fuel. In addition, the intensity ratios of spectral lines from the Lyman series of hydrogen and its isotopes and also of hydrogen-like He, He II (He^+), are often observed to be near-constant. This is unexpected and would suggest that the plasma regions emitting the radiation have similar temperatures. This contrasts with observations of, for example, C IV for which a wide range of electron temperatures of the emitting plasma region (17–65 eV) is found (Lawson *et al* 2011).

A study that in the first instance concentrates on He II is been carried out to gain a better understanding of the JET observations of the VUV Lyman series and to provide clear quantitative data for comparisons with the theoretical models. The study has considered the frequency with which near-constant line intensity ratios are observed and lists exceptions. The present paper provides a comprehensive set of measurements, which should form a useful basis for further work. Data from several spectrometers have been checked, although those from the VUV survey instruments known locally as KT2 and KT7 have proved of most use. These allow more than one member of the Lyman series to be observed at the same time, permitting line intensity ratios to be sampled throughout many pulses.

Section 2 describes the VUV instruments used to record the spectra together with the line intensity integration techniques employed and section 3 presents the measurements of the He Lyman series. All pulse surveys and examples of the time histories of line intensities throughout individual pulses are presented for several lines-of-sight, both horizontal viewing the main chamber plasma and vertical with views towards the divertor. Poloidal scans of emission across the divertor are also shown. The same, near-constant ratios occur during periods of a discharge when the He emission is comparatively low, although the precision with which the time histories of the line intensities can follow each other is nevertheless entirely unexpected. Excursions from these near-constant ratios are seen with intense He emission, which often occurs towards the end of a pulse or with significant additional heating power. Consideration has also been given to whether extreme opacity in the low temperature, high density plasmas expected in the divertors of tokamak machines may result in the Lyman observations becoming unreliable. To address this concern, comparisons with Balmer and Paschen series line members, which are not affected by opacity, are described in section 4. Section 5 provides details of the discrepancies between the He II measurements and two CR models. The conclusions are given in section 6.

2. Experimental arrangement

2.1. Spectroscopic instruments

2.1.1. The KT7 spectrometers. Two VUV diagnostics are used in spectral surveys of the JET plasmas, one observing the JET divertor, the second having a horizontal line-of-sight. Of particular importance for this study are the measurements from the KT7 spectrometers, which observe the divertor. The diagnostic consists of three separate spectrometers (Wolf *et al* 1995), a double SPRED spectrometer (Fonck *et al* 1982) and a Schwob–Fraenkel instrument (Schwob *et al* 1987). All have the same line-of-sight viewing from the top of the machine towards the divertor. The diagnostic can be tilted poloidally allowing the line-of-sight to view anywhere from the inner divertor to the scrape-off layer above the throat of the outer divertor. Many of the KT7 He spectra being analysed in the present study were recorded with a view directly into the outer divertor and also towards the target plate of the inner divertor, the line-of-sights being shown in figure 1.

The KT7 spectra analysed for the present report were recorded with the double SPRED spectrometers. These instruments are enclosed in stainless steel shielding to reduce noise due to both neutrons and γ-rays, with 15 cm of shielding between the plasma and detectors and 5 cm thickness at the back and sides. The detectors are microchannel plate (MCP)/phosphor combinations which are coupled to a Reticon photodiode array via a fibre optic bundle. It is the interaction of the neutrons and γ-rays with the MCP, with its high gain, that is of most concern. A shielding of 15 cm of steel was expected to reduce the 2.5 MeV neutron flux by a factor of $\sim$8 and that of the 8 MeV γ-rays by a factor of $\sim$17. Comparisons were made shortly after the double SPRED instrument was commissioned with the JET VUV SPRED survey spectrometer, which has a horizontal line-of-sight and is unshielded. These suggested that the background due to nuclear reaction products was a factor of $\sim$7 lower in the double SPRED instruments than in the unshielded spectrometer. The MCPs have a CuI coating in order to enhance the electron emission. The detector integration time can be varied down to a minimum of 11 ms, the readout time of the detectors, with 15–25 ms being used routinely.

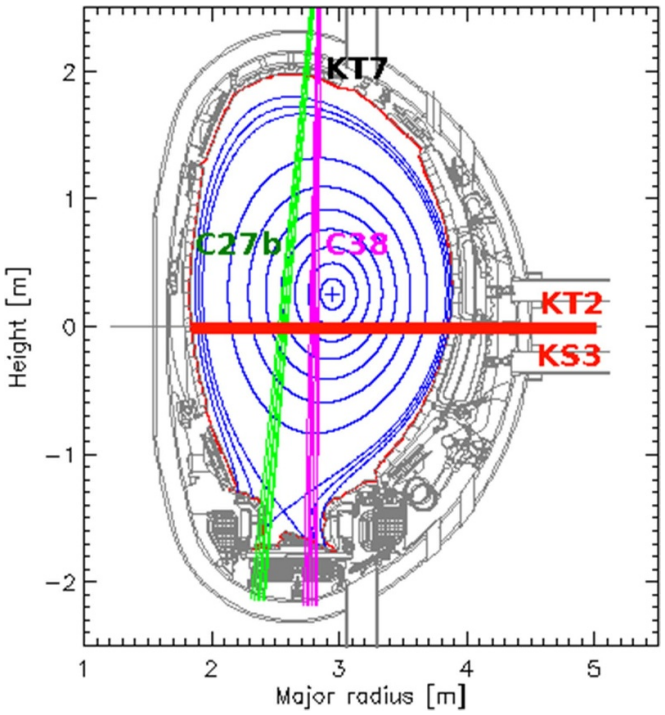

Figure 1. Lines-of-sight of the KS3, KT2 and KT7 spectrometers used during the JET C27b and C38 campaigns, together with the magnetic configuration at 17 s in pulse 93 048.

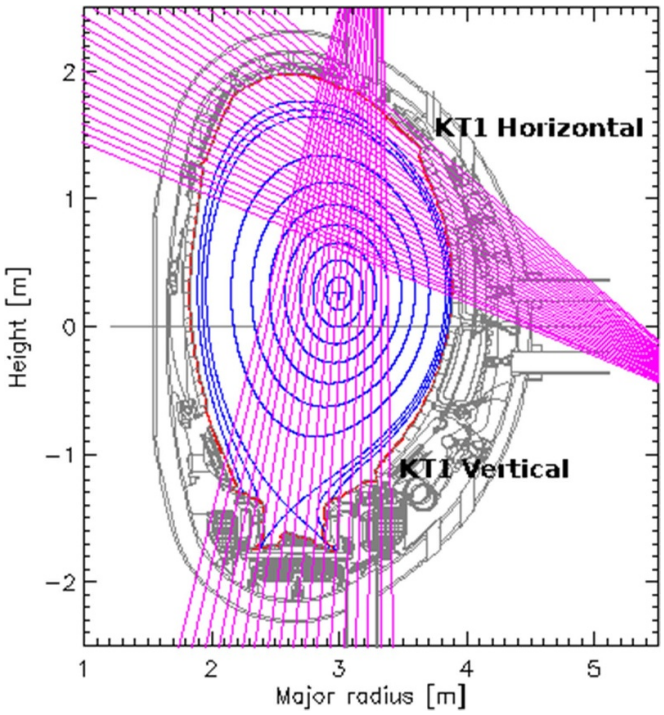

Figure 2. Lines-of-sight of the KT1 VUV spectrometers, together with the magnetic configuration at 9 s in pulse 90 379.

Both spectrometers have toroidal holographic gratings, with, respectively, ruling densities of 450 (KT7/1) and 2105 g mm^{-1} (KT7/2). They have extended and shifted spectral ranges compared with the standard SPREDs, the former observing 148–1480 Å with a spectral resolution of ∼5 Å, the latter 140–444 Å with a spectral resolution of ∼1 Å. Usually the gratings supplied with the SPREDs enhance the first and third spectral orders. In the case of the longer wavelength spectrometer (KT7/1), the second spectral order is found to be more intense than the third. Due to the combination of the wavelength coverage and the fall in sensitivity at the shortest wavelengths, higher spectral orders are less important for the short wavelength instrument.

The KT7 detectors have 2048 pixels, although a detector fault in the short wavelength detector in which adjacent pairs of pixels output the same intensity, effectively halved the useful number of pixels for this detector. In both detectors the signal from alternate pixels is processed by different amplifiers. A small mismatch in their gains for the long wavelength detector made it necessary to smooth the spectrum by averaging the intensities of adjacent pixels.

2.1.2. The KT2 spectrometer. The other VUV survey spectrometer is a standard SPRED spectrometer (Fonck *et al* 1982) with a horizontal line-of-sight (figure 1), known locally as KT2. It is remote from the machine viewing the plasma along an 18 m beamline. The instrument routinely uses a toroidal holographic grating with a ruling density of 450 g mm^{-1}. The spectral range is from ∼100–1100 Å and the spectrometer has a spectral resolution of ∼5 Å. The illuminated length of the phosphor and the fibre optic bundle that transmits light to the detector is 40 mm, the detector having 2048 pixels. The third spectral order is enhanced, although over time degradation of the grating has led to the appearance of the second order which is slowly becoming more intense. The method used to obtain the sensitivity calibration for KT2 is described by Lawson *et al* (2009). A similar approach was used for the KT7 spectrometers.

2.1.3. The KT1 spectrometers. Results recorded with a poloidally scanning spectrometer are also presented (Lawson *et al* 2012). Known locally as KT1 it covers both VUV and visible spectral ranges. There are two systems, one with a vertical line-of-sight (KT1 Vertical) which scans across the divertor and the second scanning the upper inner wall of the vessel (KT1 Horizontal) as shown in figure 2. The VUV measurements obtained with the vertical line-of-sight are of interest in the present context. The scan is achieved by a compact oscillating mirror situated outside the torus vacuum which is driven by a small motor connected to the mirror by a magnetic feedthrough. The motor is encased in a soft iron shield in order to minimize the effects of the nearby poloidal field coils on the mirror movement. Both systems use a VUV spectrometer with a 1 m, 5° grazing incidence mount. The grating has 1200 g mm^{-1} and a blaze angle of 300 Å. Each system has two detectors, each of which is able to observe a single spectral line within the range ∼200–1500 Å. Different wavelengths

Table 1. Spectrometers used in the present study.

Spectrometer	Spectral range (Å)	View	Observation
KSRA	4215–5538	Horizontal, single L-o-S	Paschen α
KT1	∼200–1500	Divertor poloidal scan	Lyman series
KT2	∼100–1100	Horizontal, single L-o-S	Lyman series
KT7/1	148–1480	Vertical, single L-o-S	Balmer γ
KT7/2	140–444	Vertical, single L-o-S	Lyman series

are accessed by moving the position of the detector around the Rowland circle of the spectrometer. The detectors consist of two back-to-back, chevron MCPs together with 16 multi-wire anodes. The front surface of each detector is coated with 0.3 μm of CuI to enhance its sensitivity. The physical size of the detectors limits the minimum separation of the two spectral lines that can be observed in any one discharge. The high intensity of the divertor emission allows a time resolution of 1 ms, with a poloidal scan taking ∼130 ms in each direction.

2.1.4. The KSRA spectrometer. It is of interest to make comparisons with higher series members and for this a visible, high resolution spectrometer, KSRA, one of the KS3 suite of instruments, is employed. The plasma is viewed along the same beamline as used by the KT2 VUV spectrometer (figure 1). The light is collected by an f/2.2 telescope containing a lens with a focal length of 50 mm and is relayed by an optical fibre to a separate room. Here the spectrum is analysed with a custom-built Czerny–Turner spectrometer, which uses a 1200 g mm^{-1} diffraction grating and 80 μm slit. A 1024 × 2048 Princeton Instruments ProEM eXcelon CCD camera is used to detect the spectrum. The spectrum covers the range 4215–5538 Å with a spectral resolution of ∼5 Å. The time resolution is limited by the detector to ∼30 ms, this resolution being used for the present measurements. The line-of-sight is shown in figure 1. Table 1 lists the spectrometers used in the present study, together with their spectral range and view, and gives the spectral lines for which they have been used.

2.2. Spectral line integration techniques

A simple and reliable spectral line integration method is usually employed for the KT2 and KT7 spectrometers in which a fixed number of pixels on either side of the line centre define an integration range and the background to be subtracted. The spectral line profile is the instrument function and this method takes advantage of the similarity of the instrument function throughout the wavelength range of the spectrometers and overcomes the difficulty of treating the unusual line profile in which intense lines develop extreme line wings (Lawson and Peacock 1988). These are due to charge spreading between the MCP and phosphor within the detector. When a line is unblended the integration is performed by Simpson's rule, a ±5 pixel range being used for KT2 and the long wavelength detector of KT7 (KT7/1) and a ±3 pixel range for the short wavelength detector of KT7 (KT7/2) with its halved number of useful pixels. These ranges cover the most intense part of the line profiles and their use minimizes the effect of blending in the VUV spectrum, which contains many spectral lines. Concentrating on the central, most intense section of the line profile is also important in that as a line becomes weaker the line wings become less evident, eventually disappearing.

When blending of lines occurs, line fitting is applied to the profile. The central part of the KT2 and KT7 spectral lines is approximately Gaussian and, although different functions have been tried in the line fitting procedures, Gaussian profiles give the best agreement with the observed spectra. The fit is performed using the IDL POWELL procedure. An example is illustrated in figure 3, which shows a typical triple Gaussian fit to the Lyman ε line at 234.35 Å, the Lyman ζ line at 232.58 Å (n = 1–7) and the blended higher series members observed in the KT7/2 spectrum for pulse 93 070 averaged between times 15.5 and 16.0 s. In this example the integrated area for the Lyman ε line is that denoted by ABC and for the Lyman ζ line by DEF.

A further consideration in analysing the KT2 and KT7 spectra is the need to correct for detector saturation. For the higher Lyman series lines to be reliably observed in the KT7/2 spectrum, the Lyman α and sometimes the Lyman β lines will often be saturated. Saturation particularly of the Lyman α line also occurs in the KT2 spectrum. In both cases a simple algorithm is used which makes use of the reproducibility of the central section of the line profile. A search is made in the same pulse for the most intense previous scan in which the line profile is unsaturated. A multiplication factor is then determined by matching this profile to the unsaturated pixels in the scan being processed. The factor is then used to reconstruct the central section of the saturated line from the unsaturated scan. The usual integration is then performed on the corrected line profile. In order to assess the accuracy of the algorithm when applied to the KT2 spectrum, the corrected intensities for the Lyman α line have been compared with the 2nd spectral order intensities. Generally, this was found to be within ∼±15% with a few excursions to higher reconstructed intensities. In the case of KT7/2, the 2nd spectral order of the Lyman α line does not fall within the wavelength range of the detector. Nevertheless, a comparison of similar pulses in which the degree of saturation was different demonstrates that

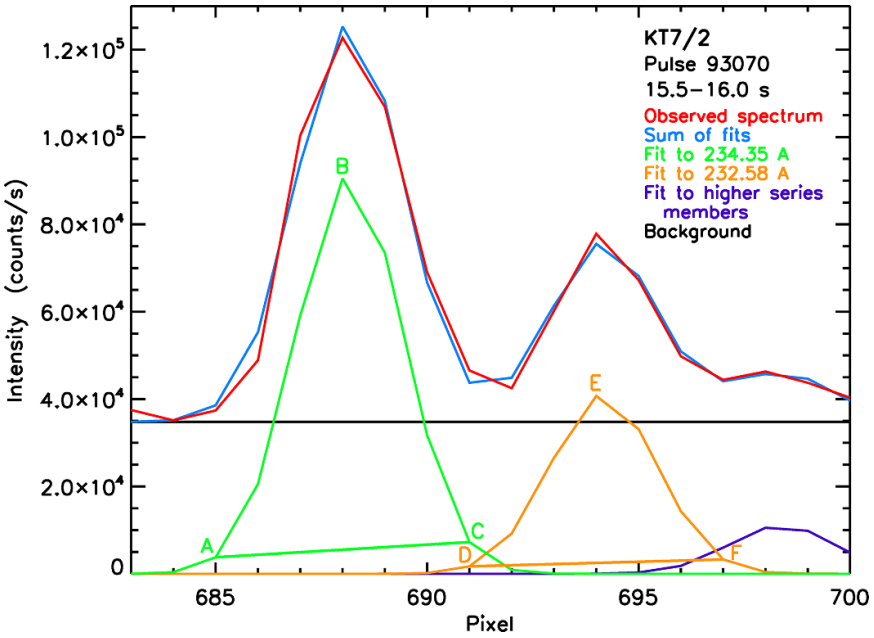

Figure 3. The spectrum of pulse 93 070 at 15.5–16.0 s recorded with KT7/2 showing a triple Gaussian fit to the 234.35 Å Lyman ε, 232.58 Å Lyman ζ lines and higher series members. ABC shows the integrated area for the Lyman ε line and DEF that for the Lyman ζ line.

the line profiles can still be reliably reconstructed. Details of an example in which there was extreme saturation in one pulse are given in section 3.4.2.

3. Lyman series results

There are several advantages of including He in this study. He fuelled plasmas tend to have fewer impurities resulting in less complex spectra, their analysis being more reliable. An example is shown in figure 4, in which the spectrum recorded by KT2 at 14 s in pulse 93 075 is shown. This spectrum is chosen so as to display weak spectral features and it can be seen that all but one line are identified with He. There are no significant populations of He molecules, ensuring that the He II excited states cannot be populated through molecular channels as happens in D fuelled discharges. In addition, He discharges are affected less by opacity than D pulses. Reabsorption of the radiation in the lowest Lyman series members due to the optical depth of the plasma can lead to a reduction in the measured line intensities. The plasma electron temperatures at which He II ions are expected are higher than those for D I. For example, Arnaud and Rothenflug (1985) give a temperature of maximum He II ion abundance of ∼4–5 eV and in non-coronal equilibrium the distribution of charge states can be described by the product of electron density and residence time, with Huber *et al* (2021) finding a somewhat higher temperature of ∼6–7 eV for a typical value of 0.3×10^{17} m^{-3}·s for this product.

He fuel was used for an experiment in the JET-ILW campaign C38. The restart of operations involving He pulses was carried out in October 2018, pulses 93 023–93 089, with the He experiment run in June 2019, pulses 93 847–93 908. Data are also available for He fuelled experiments during the JET-C operations and examples from the latest of these are presented. These experiments formed part of the C27b campaign, which was run from August to October 2009. The He restart included pulses 78 907–78 994, with the He campaign pulses following immediately and continuing up to pulse 79 243. Table 2 details the campaigns during which data used in the present paper were recorded. As explained in section 3.2, the range of plasma parameters used in the C38 restart was more limited than in many JET experiments, in particular there being no additional heating. However, inclusion of the C38 experiment and the C27b campaign in this study allows a wider range of parameters to be assessed, these being typical of many JET experiments.

3.1. All pulse surveys during the JET-ILW He restart

3.1.1. KT2 observations. The spectral resolution of KT2 limits the number of He Lyman series members that can be readily accessed to just the Lyman α and β lines at 303.78 and 256.32 Å, respectively (figure 4). The intensity of the Lyman γ line at 243.03 Å can be determined by line fitting; a double Gaussian fit is used in which one Gaussian is used to represent the 243.03 Å line and the other the Lyman δ at 237.33 Å line which is blended with higher Lyman series members. As discussed in section 2.2, the Lyman α and sometimes the Lyman β lines observed by KT2 are saturated due to the saturation of the detector. An algorithm has been developed that allows the line profile to be reliably reconstructed during the periods of saturation.

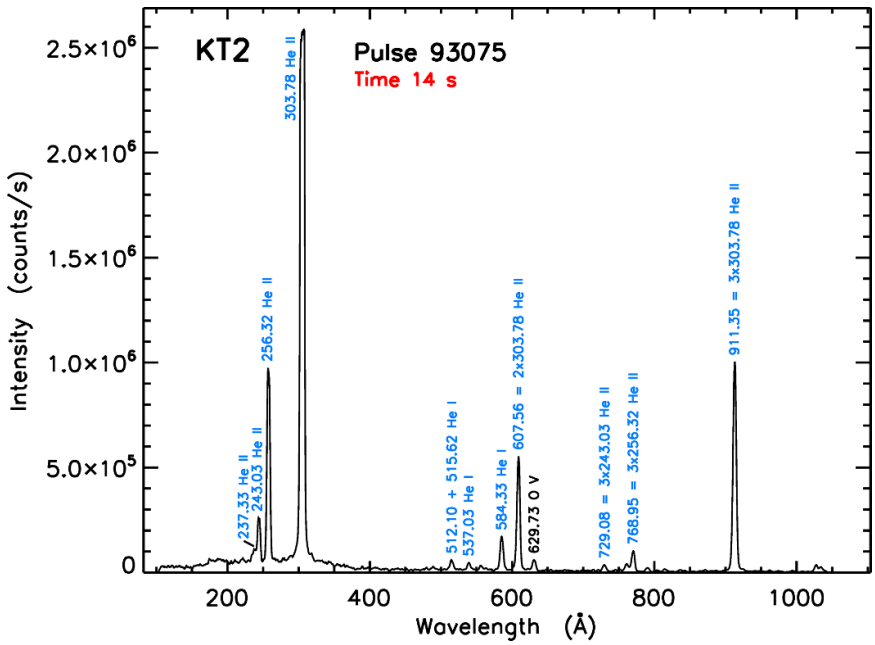

Figure 4. The spectrum of pulse 93 075 at 14 s recorded with KT2, chosen so as to display weak spectral features. The Lyman α line is saturated but can be reliably reconstructed as described in section 2.2.

Table 2. JET campaigns from which data are used.

Campaign	Dates	Pulses	KT7 line-of-sight
C27b	August–October 2009	78 885–79 853	Inner divertor target plates
C28	August–December 2011	80 128–81 643	Outer divertor throat
C36	January–May 2016	89 476–90 797	Outer divertor throat
C37	June–July 2016	90 806–91 276	Outer divertor throat
C37	1 August 2016	91 277–91 294	Central divertor tile 5
C37	2 August–24 August 2016	91 295–91 630	Outer divertor throat
C37	25 August–2 September 2016	91 631–91 756	Central divertor tile 5
C36b	28 September–8 October 2016	91 757–91 957	Central divertor tile 5
C36b	10 October–11 November 2016	91 958–92 468	Outer divertor throat
C36b	14 November–15 November 2016	92 469–92 504	Central divertor tile 5
C38	3 May–4 May 2018	92 671–92 693	Central divertor tile 5
C38	8 May 2018–December 2019	92 694–96 563	Outer divertor tile 5

Ratios of the Lyman α to β line intensities during the He restart recorded with KT2 with its horizontal line-of-sight are shown in figure 5. Each point in the plot shows the ratio of the line intensities averaged over half second intervals throughout each pulse, starting at 1.0 s with the last time interval beginning at 29.0 s. A minimum intensity of the 303.78 Å line was set to ensure a reliable integration for both lines. It is evident that the ratio is near-constant except for a few points in five pulses out of a total of 54 pulses. A few outlying points, which correspond to the last time slice in a pulse, have been removed from this figure. Rapidly changing intensities during the half second measurement period which falls in the current ramp-down lead to unreliable values of the ratios.

An overview of all the measured Lyman line intensity ratios taken from plots such as the one shown in figure 5 for the three periods of operations is given in table 3. Once the accuracy of the measurements is taken into account it can be seen that the results for KT2 are essentially the same for all three periods. The accuracy of the line integration is typically within $\pm 10\%$ and this value is used for the Lyman α to β ratio. It corresponds approximately to the spread in the data. A larger error bar is used for the Lyman α and β to γ ratios, since the Lyman γ intensity is derived from line profile fitting. The pulses which include points deviating from the near-constant ratios are listed in table 4.

3.1.2. KT7/2 observations. Figure 6 shows the KT7/2 spectrum for pulse 93 075 averaged over the time interval 16.5–17.0 s. This spectrum is chosen in order to display as much of the Lyman series as possible, despite the Lyman α line being saturated. Again, He entirely dominates the spectrum,

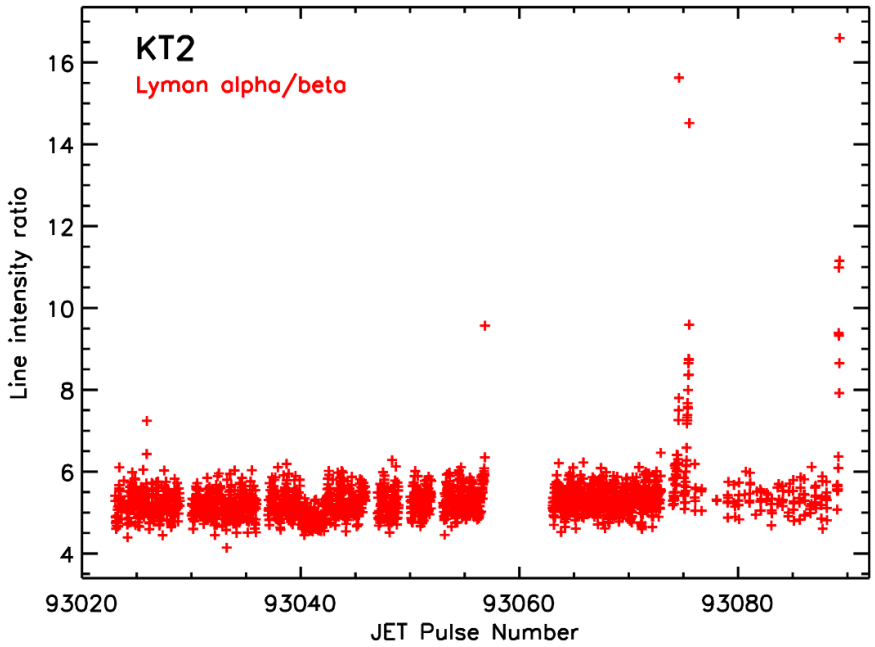

Figure 5. The Lyman α to β ratio recorded with KT2 during the JET-ILW C38 He restart, with a minimum Lyman α intensity of 8.6×10^{18} ph $(\mathrm{s{\cdot}m^2{\cdot}sr})^{-1}$.

Table 3. Measured He Lyman series line intensity ratios.

Campaign	JET-C	JET-ILW (Restart)	JET-ILW (Experiment)
Pulses	78 907–79 243	93 023–93 089	93 847–93 908
KT2			
α/β	6.40 ± 10%	5.28 ± 10%	5.20 ± 10%
α/γ	26.2 ± 15%	21.1 ± 15%	20.7 ± 15%
β/γ	4.10 ± 15%	3.99 ± 15%	3.98 ± 15%
KT7/2			
α/β	5.95 ± 10%	5.45 ± 10%	5.13 ± 10%
α/γ	23.0 ± 10%	19.5 ± 10%	18.2 ± 10%
β/γ	3.86 ± 10%	3.58 ± 10%	3.54 ± 10%
α/δ	68.3 ± 10%	51.0 ± 10%	46.4 ± 10%
β/δ	11.48 ± 10%	9.35 ± 10%	9.04 ± 10%
α/ε	186 ± 15%	178 ± 10%	151 ± 10%
β/ε	31.3 ± 15%	32.6 ± 10%	29.4 ± 10%
α/(fitted) ζ	660 ± 20%	399 ± 15%	475 ± 15%
β/(fitted) ζ	111 ± 20%	73.3 ± 15%	92.6 ± 15%

but with the spectrometer's higher spectral resolution more lines of the He Lyman series can be observed, up to the Lyman ζ ($n = 1$–7) line. The KT7/2 spectrometer had a vertical view into the outer divertor during the C38 restart and experiment (figure 1). There is more variation in the Lyman α to β ratio (303.78/256.32 Å), shown in figure 7, than observed along the KT2 spectrometer's horizontal view, although within errors this ratio is again near-constant. Further, the value of the ratio, given in table 3, is the same as for the horizontal view suggesting that the ratio does not depend on the line-of-sight; that is the divertor view is not exceptional. In this case eight pulses have points which differ from the near-constant ratio and are listed in table 4. One of these exceptional pulses has low ratios, which is expected to be due to opacity. The observation of opacity in these discharges will be discussed in a future paper.

Both the Lyman α and, less frequently, the Lyman β lines observed with KT7/2 can saturate and the same algorithm as used for the KT2 saturated lines was used to reconstruct the line profiles. In this case it was not possible to confirm the reconstruction by using the second order spectrum as was done for KT2 and a check on the algorithm used for the reconstruction in the KT7/2 spectrum is described in section 3.4.2.

The value of the ratio can be affected by the sensitivity of the integration to the line profiles, since there are relatively few pixels forming the KT7/2 profiles due to the detector fault in which adjacent pairs of pixels output the same intensity. This is seen in the Lyman β to γ ratio (256.32/243.03 Å) shown in figure 8. Again this ratio is seen to be near-constant, its value given in table 3, with the five pulses listed for KT2 in table 4 having points which deviate from this value. However, there is a tendency for the points to fall into two bands and this is due to small variations in the line profiles, as shown in figure 9. With so few pixels in the line profile, the profile being entirely due to the instrument function, these are sufficient to affect the value of the line integration. The most likely explanation for changes in the line profiles at different times within a pulse are variations in the magnetic fields around the detector; the fields can have a small effect on the paths of the electrons emitted from the detector's MCP as they travel towards the fibre optic bundle. Nevertheless, the differences between the two bands is small, ~6%, well within the integration accuracy of ±10%.

Figure 10 shows the Lyman β to δ ratio (256.32/237.33 Å), which again is seen to be near-constant. The same pulses are

Table 4. Exceptional pulses that deviate from the near-constant ratios.

Campaign	JET-C	JET-ILW (Restart)	JET-ILW (Experiment)
Pulses	78 907–79 243	93 023–93 089	93 847–93 908
KT2			
	79 059, 79 073, 79 074	93 025	93 865, 93 870
	79 111, 79 112, 79 113	93 056	93 894, 93 895
	79 115, 79 128, 79 155	93 074	93 896, 93 897
	79 162, 79 164, 79 167	93 075	93 898, 93 899
	79 168, 79 172, 79 181	93 089	93 900, 93 902
	79 183, 79 205		
KT7/2			
	78 913, 78 914, 78 965	93 023	93 867, 93 868, 93 869
	79 008, 79 014, 79 017	93 025	93 870, 93 871, 93 872
	79 073, 79 074, 79 076	93 048	93 873, 93 874, 93 875
	79 097, 79 099, 79 105	93 051	93 879, 93 893, 93 894
	79 111, 79 112, 79 113	93 056	93 895, 93 896, 93 897
	79 114, 79 162, 79 164	93 074	93 898, 93 899, 93 900
	79 167, 79 168, 79 169	93 075	93 901, 93 902, 93 908
	79 170, 79 171, 79 237	93 078 (β/δ)	
	79 240, 79 241, 79 242	93 089	

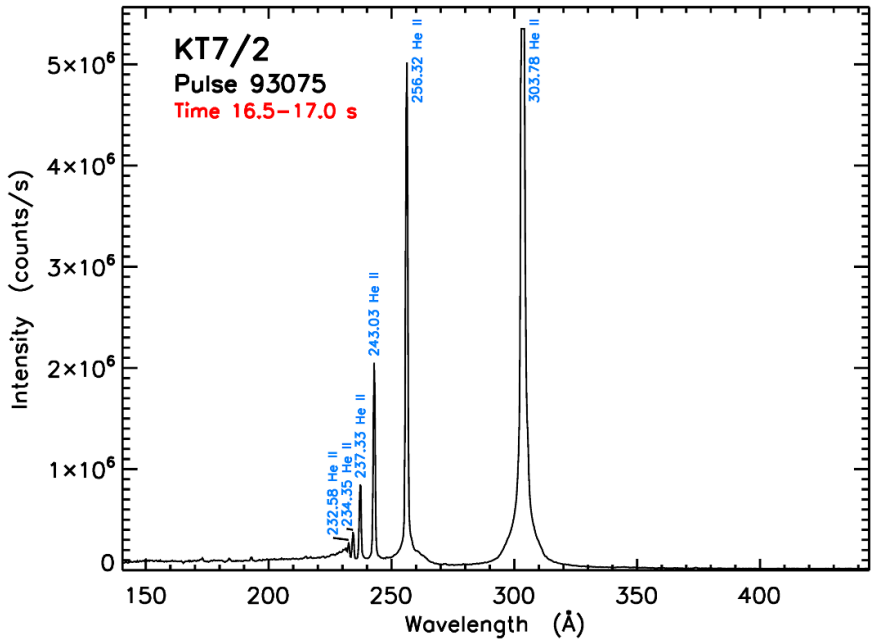

Figure 6. The spectrum of pulse 93 075 averaged between 16.5–17.0 s recorded with KT7/2, chosen to display the He Lyman series. Although saturated the Lyman α line can be reliably reconstructed.

seen to be exceptional in this plot, although additionally pulse 93 078 shows a marked excursion.

It is necessary to use line fitting to determine reliable intensities of the Lyman ζ line at 232.58 Å. In this case, the fit uses a triple Gaussian fit to the Lyman ε line at 234.35 Å, the Lyman ζ line and the blended higher series members (figure 3). Integrating the fitted Lyman ε line profiles gave results which were similar to the line integration carried out on the unfitted profiles. Typically, the fitted line intensities tended to be ∼5% lower than those given by the integration of the unfitted profiles. Since data using the unfitted profiles are available for all pulses and are closer to the method used for the integration of the Lyman β line, the unfitted line integrations have been used in generating the Lyman β to ε ratio shown in figure 11. The intensity derived from the fitted Lyman ζ line is used in figure 12. The data are sparser in this figure since the line profile fitting was only achieved for the most intense He spectra. Deviations from the generally near-constant ratio observed in

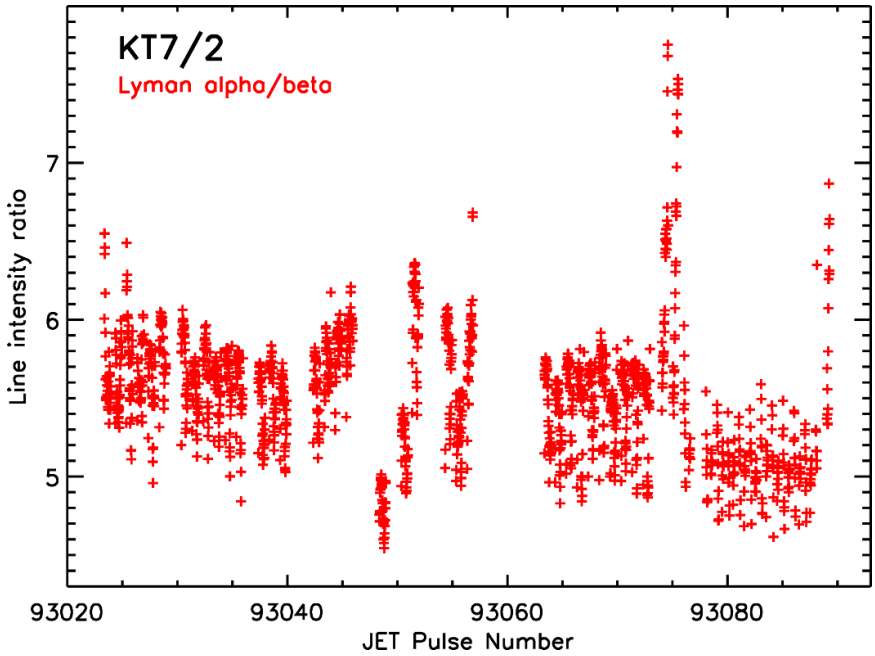

Figure 7. The Lyman α to β ratio recorded with KT7/2 during the JET-ILW C38 He restart, with a minimum Lyman α intensity of 7×10^{19} ph $(\mathrm{s{\cdot}m^2{\cdot}sr})^{-1}$.

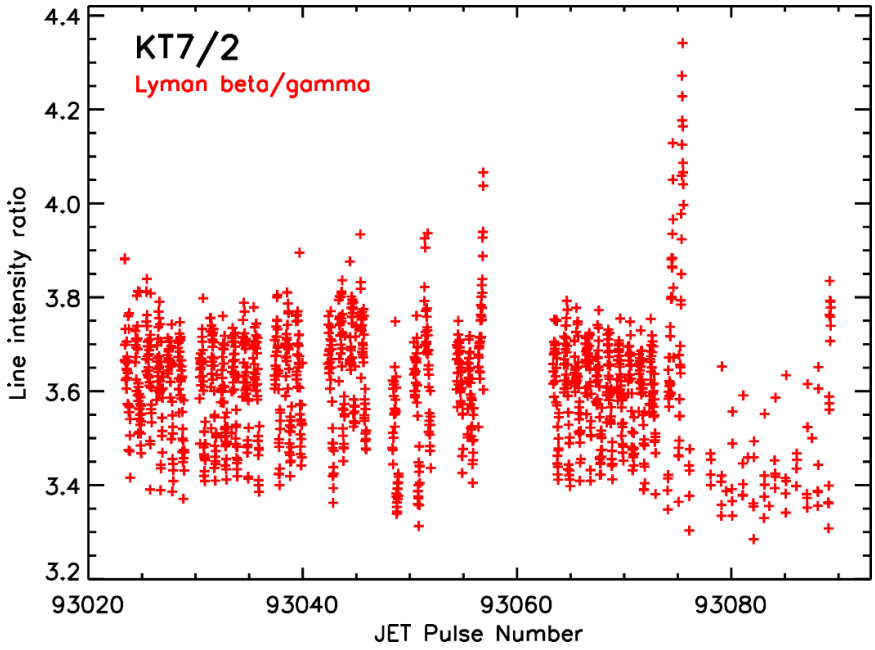

Figure 8. The Lyman β to γ ratio recorded with KT7/2 during the JET-ILW C38 He restart, with a minimum Lyman α intensity of 1.4×10^{20} ph $(\mathrm{s{\cdot}m^2{\cdot}sr})^{-1}$.

both figures 11 and 12 are seen for the same pulses as found for the other ratios.

3.2. All pulse surveys during the JET-ILW He experiment and JET-C He campaign

It is clear from the above figures that the Lyman series line ratios tend to be near-constant apart from a few exceptional pulses. Nevertheless, it should be recognized that the range of plasma parameters that occurred during the He restart was smaller than is usual in JET campaigns. The toroidal field ranged from 0.9 to 3.0 T, but the maximum plasma current used was only 1.8 MA. The maximum electron temperatures and densities varied between 0.53–4.4 keV and 2.0×10^{18} to 8.8×10^{19} m^{-3}, respectively, with radiated powers of up to 2.7 MW recorded. Of particular note is that no additional

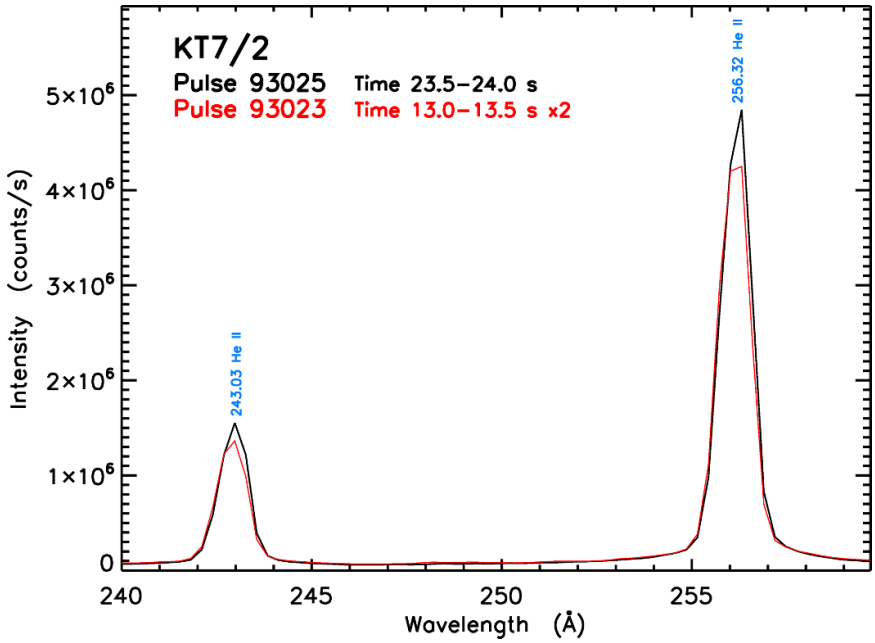

Figure 9. A comparison of line profiles in the spectra of pulses 93 025 and 93 023 recorded with KT7/2.

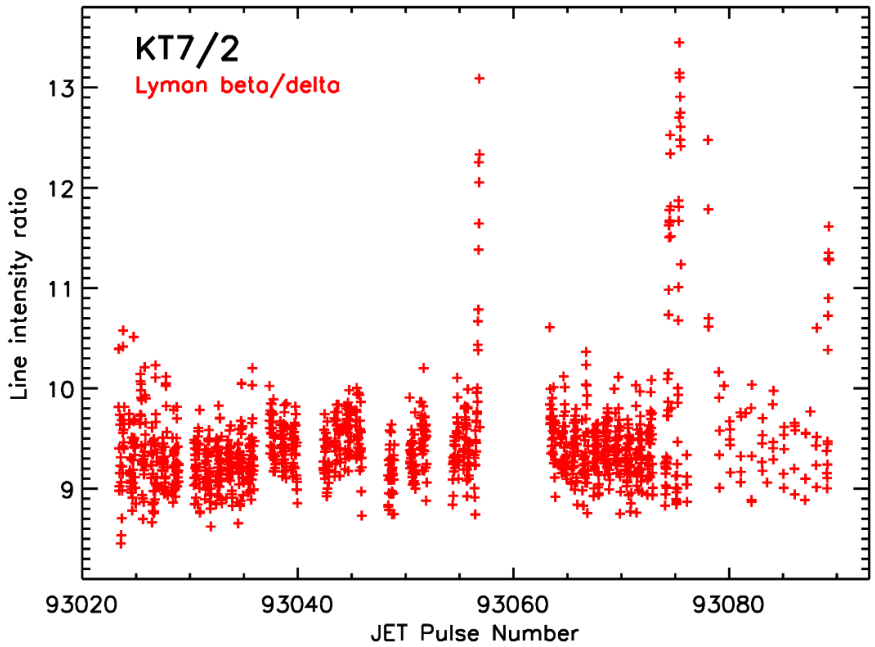

Figure 10. The Lyman β to δ ratio recorded with KT7/2 during the JET-ILW C38 He restart, with a minimum Lyman α intensity of 1.4×10^{20} ph $(\mathrm{s{\cdot}m^2{\cdot}sr})^{-1}$.

heating was used during this restart period. Consequently, it is important to include the C38 He experiment in this study and He discharges from the JET-C C27b campaign. In both of these additional heating was used, there also being a wider range of plasma parameters. In the C38 He experiment additional heating included up to 10.6 MW of D NBI and 6.0 MW of ICRH. Somewhat higher plasma currents of 2 MA were used with maximum electron temperatures and densities reaching 5.1 keV and 1.0×10^{20} m^{-3}, respectively, with radiated powers up to 5.8 MW. In JET-C C27b, He NBI was used with powers reaching 16.2 MW and ICRH again delivering up to 6.0 MW of power. Although the maximum electron temperature was similar at 5.8 keV, higher maximum electron densities and plasma currents of 1.4×10^{20} m^{-3} and 2.6 MA, respectively, were measured. Higher radiated powers of 7.7 MW were also observed. Although not reaching the very highest values

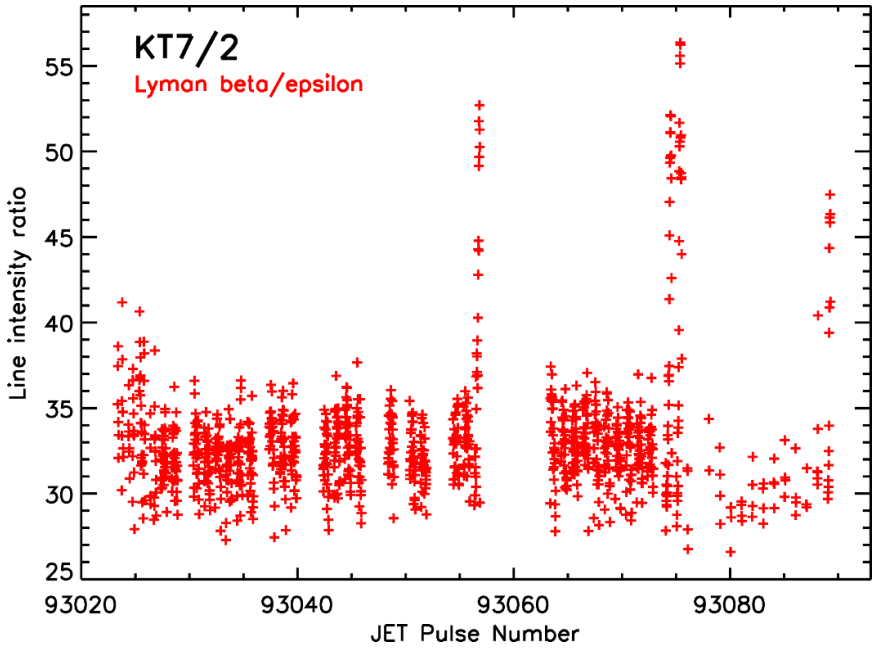

Figure 11. The Lyman β to ε ratio recorded with KT7/2 during the JET-ILW C38 He restart, with a minimum Lyman α intensity of 2.1×10^{20} ph$(\mathrm{s{\cdot}m^2{\cdot}sr})^{-1}$.

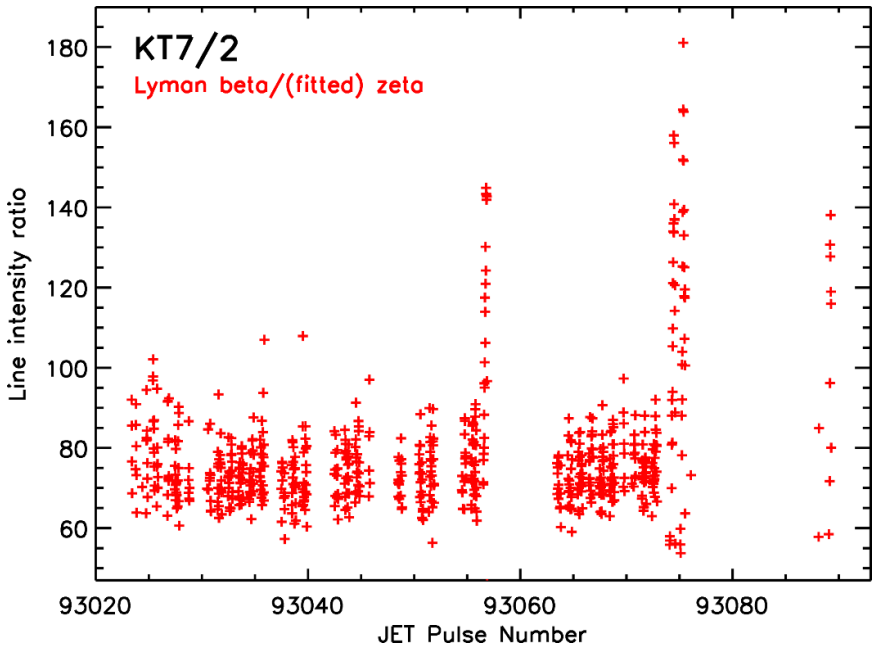

Figure 12. The Lyman β to (fitted) ζ ($n = 1$–7) ratio recorded with KT7/2 during the JET-ILW C38 He restart, with a minimum Lyman α intensity of 3.2×10^{20} ph $(\mathrm{s{\cdot}m^2{\cdot}sr})^{-1}$.

of these parameters recorded on JET, these ranges nevertheless cover values typical of many JET experiments.

3.2.1. KT2 observations. Figures 13 and 14 show the Lyman α to β ratio (303.78/256.32 Å) recorded with KT2 for the JET-ILW He experiment and the JET-C He campaign, respectively. The more varied operating conditions led to more exceptional points in these datasets. However, a number of these correspond to rapidly changing plasma conditions or impurity influxes distorting the spectra. In figure 13 the high points in pulse 93871 are due to a rapid and strong increase in the He emission immediately before the pulse termination. In pulses 93 872–93 875 the Lyman ratio is affected by W influxes around 54–56 s. So as improve clarity in this figure some points have been removed. For example, poor terminations in 11 pulses resulted in MARFE-like emission. This rapidly varying radiation led to a range of Lyman ratios which

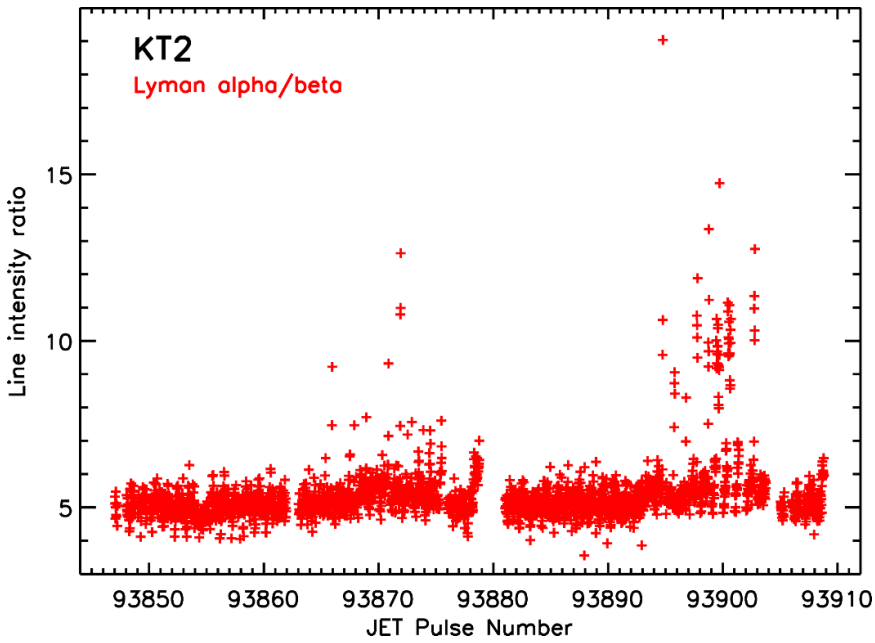

Figure 13. The Lyman α to β ratio recorded with KT2 during the JET-ILW C38 He experiment, with a minimum Lyman α intensity of 8.6×10^{18} ph $(\mathrm{s{\cdot}m^2{\cdot}sr})^{-1}$.

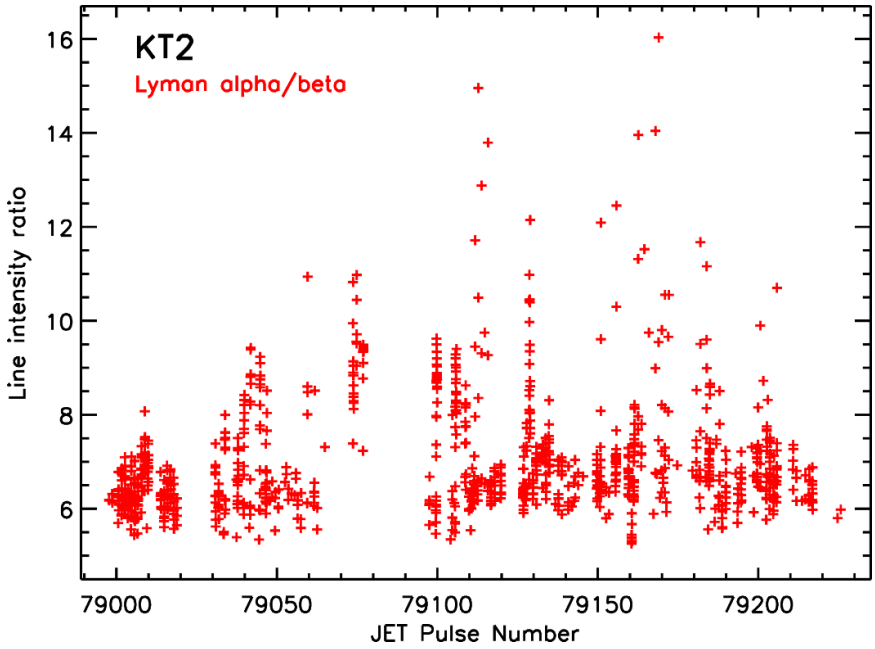

Figure 14. The Lyman α to β ratio recorded with KT2 during the JET-C C27b He campaign, with a minimum Lyman α intensity of 2×10^{19} ph $(\mathrm{s.m^2.sr})^{-1}$ and minimum He/C ratio of 9.2.

are not considered reliable. Most of the other outlying points were found to occur at the end of discharges where conditions are also changing rapidly, this accounting for the removal of the last time slices of a further three pulses. After allowing for all the points that are regarded as unreliable, there are still 10 exceptional pulses with particularly high ratios out of a total of 58 pulses. These are listed in table 4 and correlate with periods of intense He emission. Nevertheless, the values of the Lyman α to β ratio in the majority of time slices can be seen to be near-constant and are given in table 3.

The data shown in figure 14 for the C27b He campaign include a wider range of pulses, covering a variety of different scenarios. There are more cases in which the ratios are regarded as being unreliable, but also more cases in which the ratios are thought to be reliable, although differ from a near-constant value. Of those considered unreliable, 51 points in 40 different pulses have been removed from figure 14, since the discharge ends in a disruption or ragged termination, both of which affect the Lyman ratios. 20 points from 9 pulses are extreme due to particularly strong He influxes or rapidly

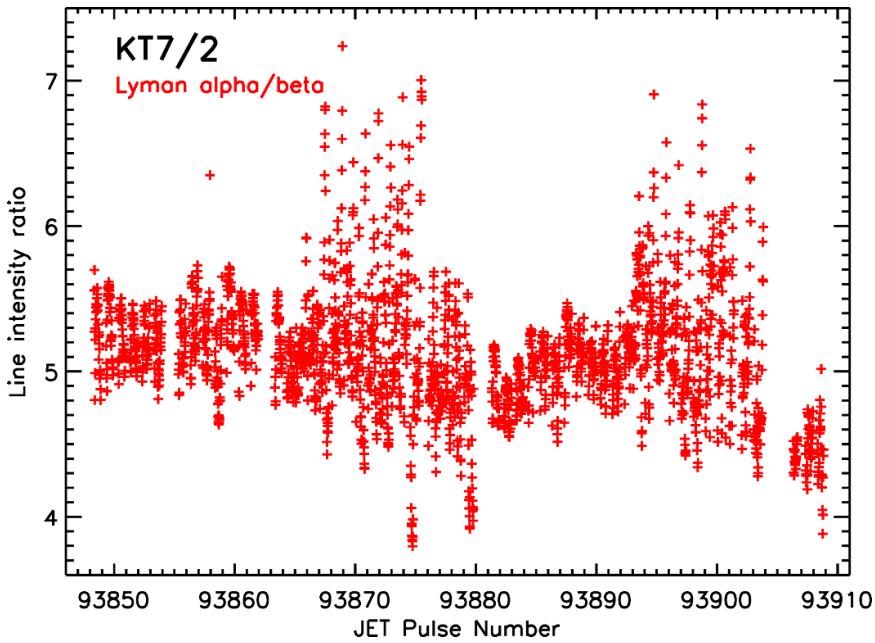

Figure 15. The Lyman α to β ratio recorded with KT7/2 during the JET-ILW C38 He experiment, with a minimum Lyman α intensity of 1.2×10^{20} ph $(\mathrm{s{\cdot}m^2{\cdot}sr})^{-1}$.

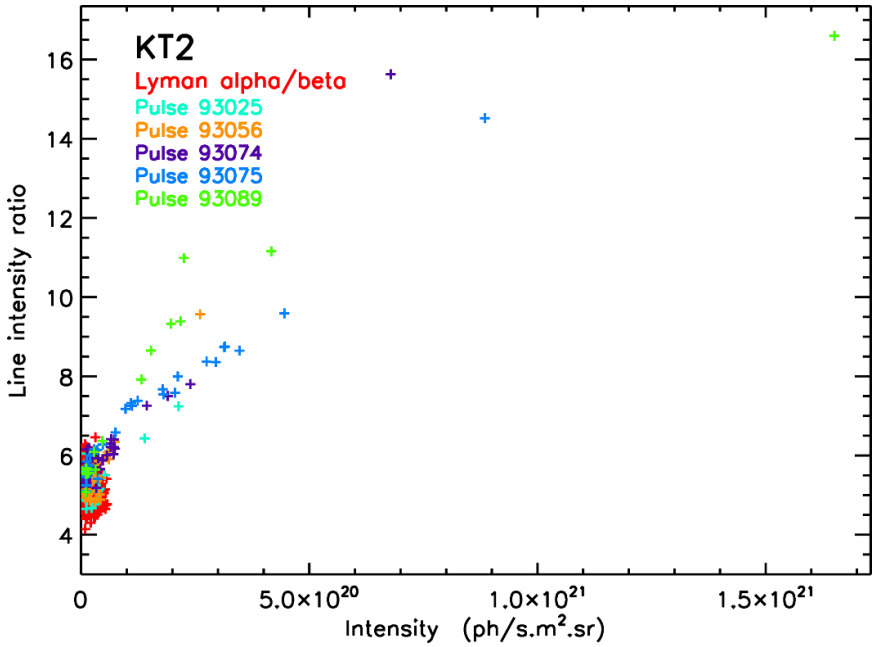

Figure 16. The Lyman α to β ratio against the Lyman α intensity recorded with KT2 during the JET-ILW C38 He restart, with a minimum Lyman α intensity of 8.6×10^{18} ph $(\mathrm{s{\cdot}m^2{\cdot}sr})^{-1}$.

changing He intensities and have been removed. In addition, 17 points from 6 pulses are unreliable due to metallic influxes (Ni, Cu and Fe) and a point from each of 2 pulses due C influxes. Also of note is that the Lyman β line in the KT2 spectrum can be affected by the C V feature at 248.7 Å and so a minimum He Lyman β to 977.02 Å C III line intensity ratio was set for points to be included in this figure. Of the remaining dataset of just over 200 pulses many more pulses ($\sim$45%) have some points which differ from the background of the near-constant ratio, which nevertheless is evident. In nearly half of these an increase was seen in the ratio towards the end of the discharge, this corresponding to an increase in the He intensity. The Lyman γ line is also blended with a C line, the C IV line at 244.91 Å. Consequently, only spectra with a high He to C ratio were used in the line fitting program to determine ratios with the Lyman γ line. The resulting near-constant ratios, listed in table 3, match those found for the other spectrometer and operational periods. 17 pulses with marked excursions from these near-constant ratios are given in table 4.

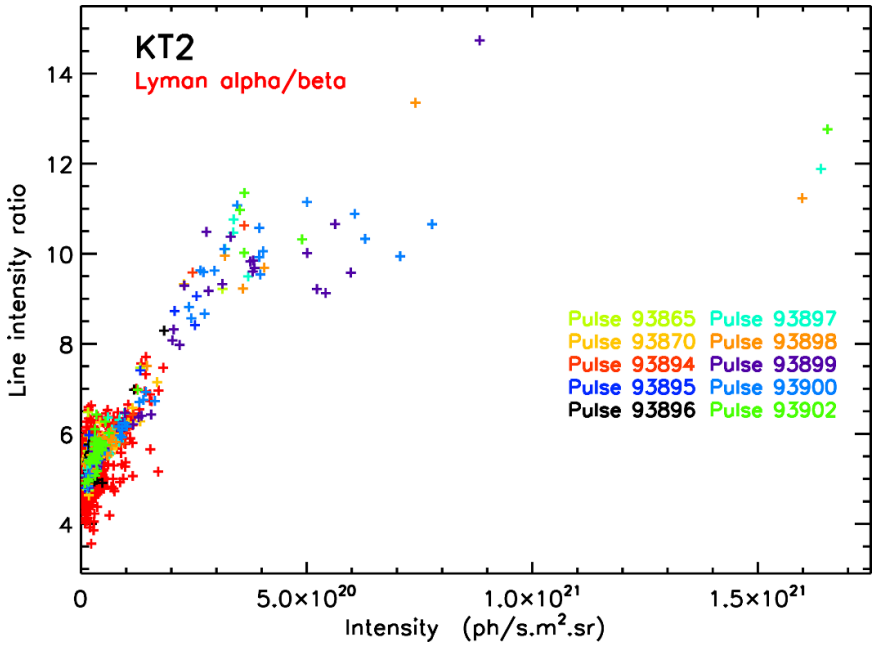

Figure 17. The Lyman α to β ratio against the Lyman α intensity recorded with KT2 during the JET-ILW C38 He experiment, with a minimum Lyman α intensity of 8.6×10^{18} ph $(\mathrm{s{\cdot}m^2{\cdot}sr})^{-1}$.

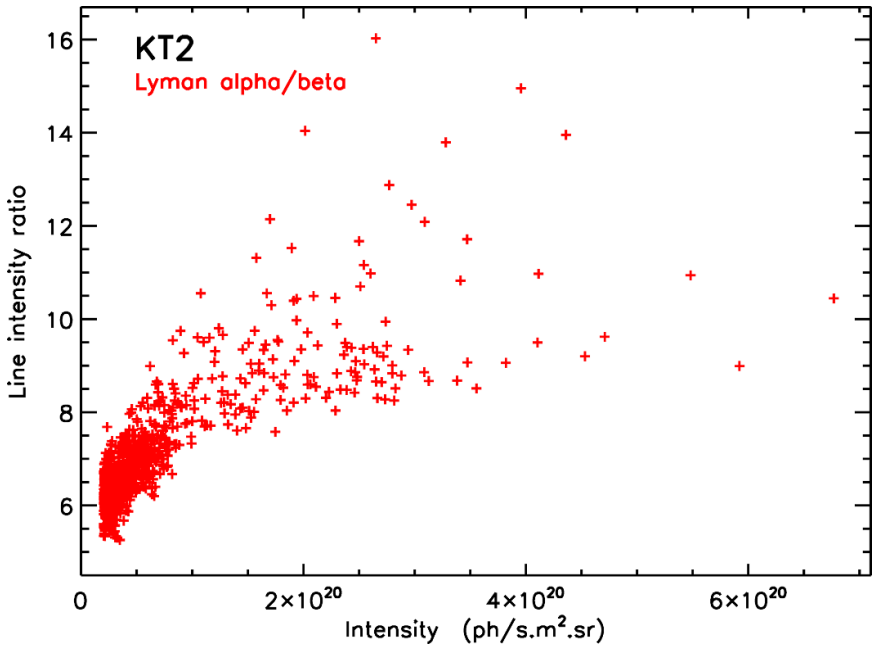

Figure 18. The Lyman α to β ratio against the Lyman α intensity recorded with KT2 during the JET-C C27b He campaign, with a minimum Lyman α intensity of 2×10^{19} ph $(\mathrm{s{\cdot}m^2{\cdot}sr})^{-1}$and minimum He/C ratio of 9.2.

3.2.2. KT7/2 observations. Plots of the Lyman ratios generated from KT7/2 data for the JET-ILW C38 He experiment and JET-C C27b He campaign show similar trends to those already illustrated. During C38, KT7/2, with its vertical view towards the divertor, had a line-of-sight onto the outer divertor tile 5 and in the C27b He campaign it viewed the inner divertor target plates (figure 1). Values of the observed near-constant ratios are again given in table 3 and pulses with exceptional values of the ratios in table 4. The ratios for the JET-C He campaign tend to be higher than for the JET-ILW pulses, with that for the Lyman β to δ ratio being marginally outside the expected errors. The spread in the data for the Lyman β to ε ratio was larger than was found for the other ratios with a larger error bar thought appropriate. As before the Lyman ζ line profile was determined by fitting and the spread in the data for Lyman β to fitted ζ line ratio was large with a consequent higher error bar for this ratio. A plot of the Lyman α to β ratio for the JET-ILW C38 He experiment is shown in figure 15. Other Lyman series ratios are illustrated by Lawson *et al* (2022).

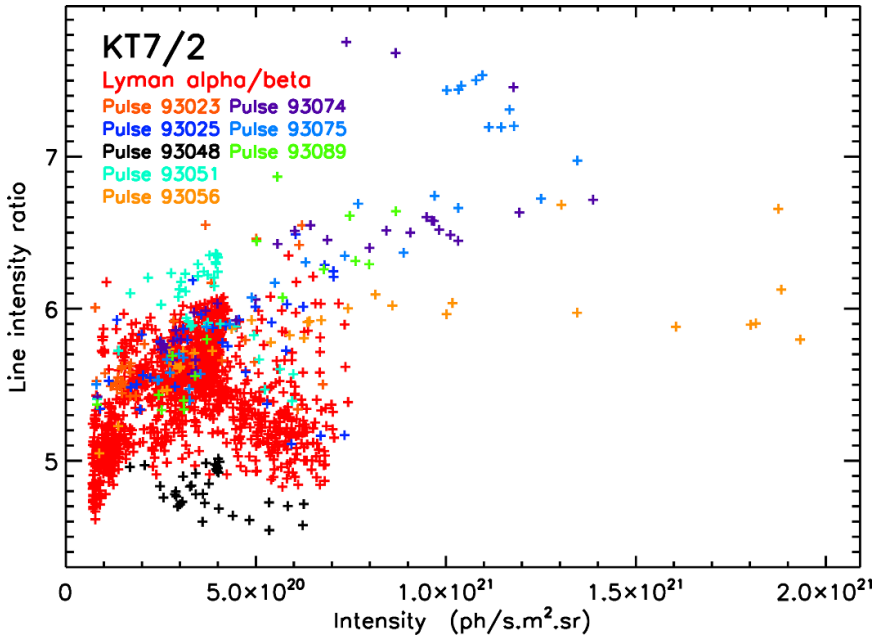

Figure 19. The Lyman α to β ratio against the Lyman α intensity recorded with KT7/2 during the JET-ILW C38 He restart, with a minimum Lyman α intensity of 7×10^{19} ph $(\mathrm{s{\cdot}m^2{\cdot}sr})^{-1}$.

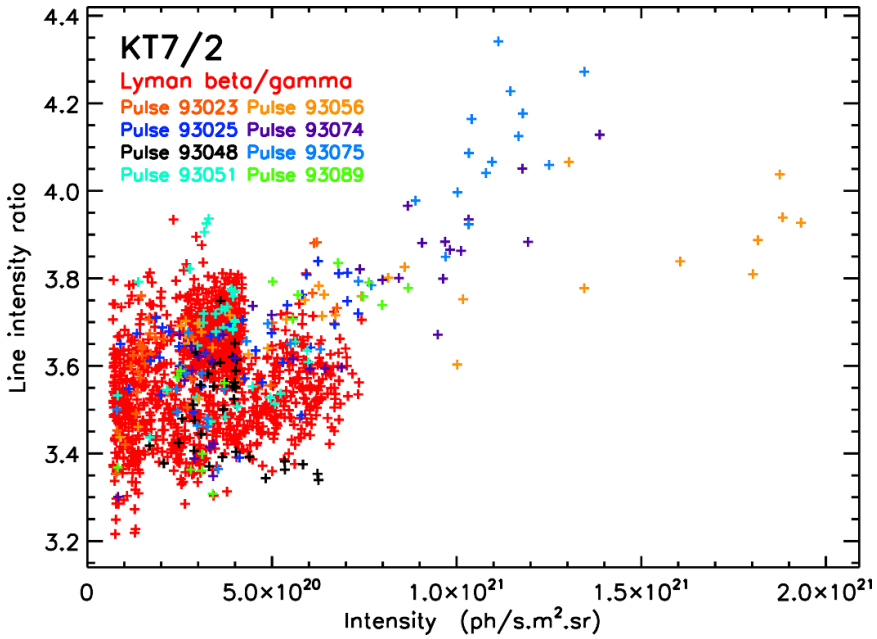

Figure 20. The Lyman β to γ ratio against the Lyman α intensity recorded with KT7/2 during the JET-ILW C38 He restart, with a minimum Lyman α intensity of 7×10^{19} ph $(\mathrm{s{\cdot}m^2{\cdot}sr})^{-1}$.

3.3. Dependence of the Lyman ratios on the Lyman line intensities

The intense He emission seen in many of the pulses in which the Lyman ratios deviate from the near-constant ratios suggests a correspondence between high Lyman ratios and high levels of He. Figures 16–18 show the Lyman α to β ratio observed with the KT2 spectrometer plotted against the Lyman α intensity for the JET-ILW He restart and experiment and the JET-C He campaign, respectively. Although the bulk of the points fall in a narrow range, these data confirm the correlation between the exceptional Lyman α to β ratios and the Lyman α intensity.

However, data recorded with KT7/2 with its view into the divertor show a more complicated picture. Figure 19 shows the KT7/2 Lyman α to β ratio plotted against the Lyman α intensity for the C38 restart. Although a correspondence between high ratios and high intensities can still be seen (above a Lyman α intensity of $\sim 7.5 \times 10^{20}$ ph $(\mathrm{s{\cdot}m^2{\cdot}sr})^{-1}$ the only exception is pulse 93 056), there is also a branch of points

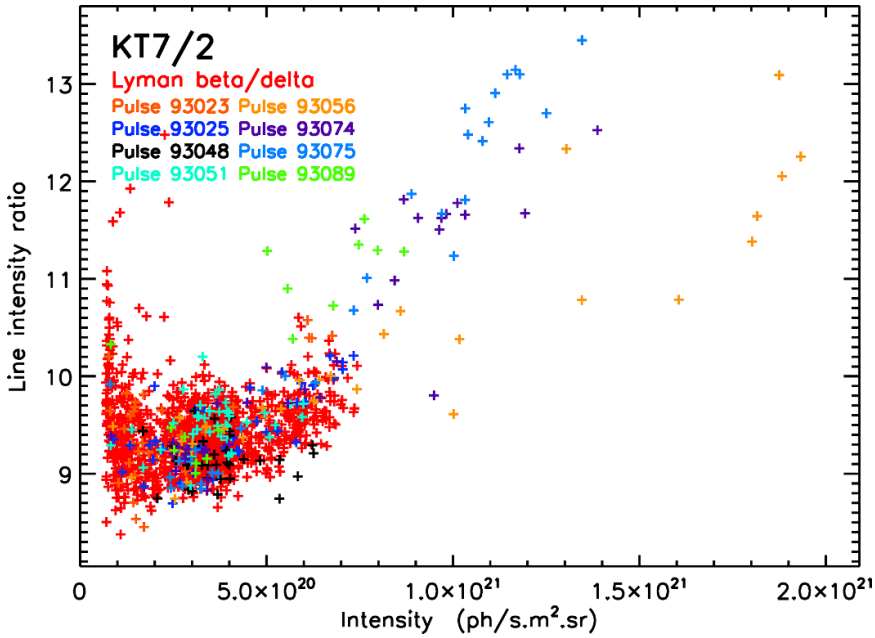

Figure 21. The Lyman β to δ ratio against the Lyman α intensity recorded with KT7/2 during the JET-ILW C38 He restart, with a minimum Lyman α intensity of 7×10^{19} ph $(\mathrm{s{\cdot}m^2{\cdot}sr})^{-1}$.

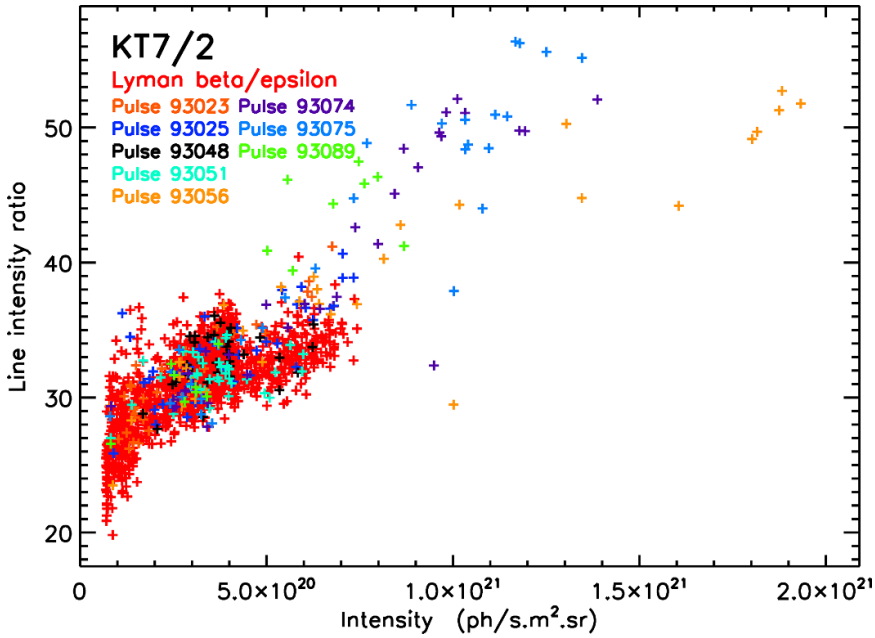

Figure 22. The Lyman β to ε ratio against the Lyman α intensity recorded with KT7/2 during the JET-ILW C38 He restart, with a minimum Lyman α intensity of 7×10^{19} ph $(\mathrm{s{\cdot}m^2{\cdot}sr})^{-1}$.

which above a Lyman α intensity of $\sim 4 \times 10^{20}$ ph $(\mathrm{s{\cdot}m^2{\cdot}sr})^{-1}$ show an anti-correlation. The anti-correlation is less evident if the Lyman β to γ ratio is plotted against the Lyman α intensity, as in figure 20. This suggests opacity as a likely cause, the Lyman α line being most affected by opacity.

In making comparisons of the observations with the theoretical CR models the higher spectral resolution of KT7/2, which allows more Lyman series members to be observed, is of particular value. The dependence of the ratios on the He line intensities should also be taken into account. Consequently, ratios at a particular Lyman α intensity are determined and are listed in table 5 for the C38 He restart and experiment, these datasets being regarded as the most reliable. The values of these ratios are found from plots which for the C38 He restart are shown in figures 19–23. Similar plots for the C38 He experiment are included in Lawson *et al* (2022). A Lyman α intensity of 3.5×10^{20} ph $(\mathrm{s{\cdot}m^2{\cdot}sr})^{-1}$ is chosen; this is below the intensity at which opacity may affect the results. Apart from the Lyman β to ζ ratio for the C38 He experiment there is good agreement between the values in tables 3 and 5.

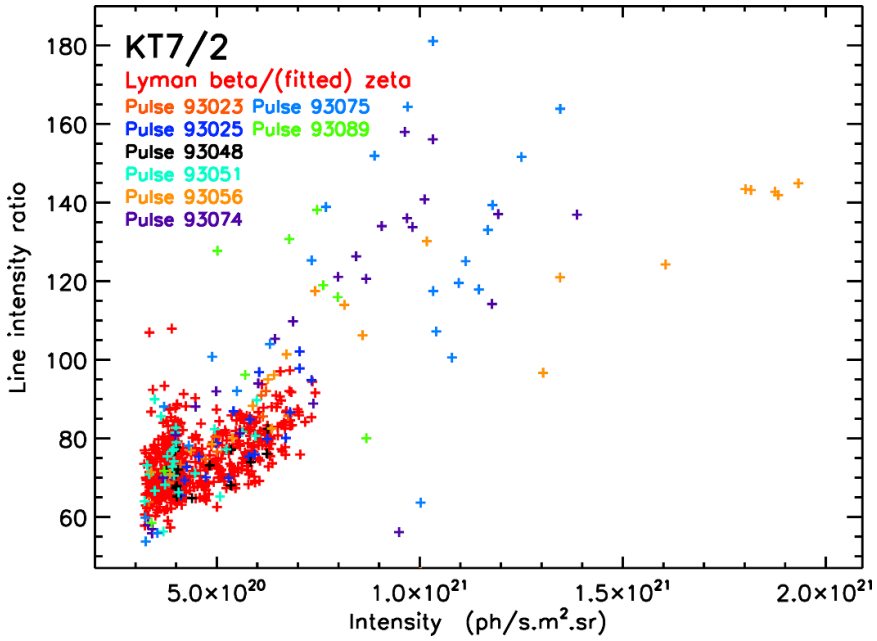

Figure 23. The Lyman β to (fitted) ζ ($n = 1$–7) ratio against the Lyman α intensity recorded with KT7/2 during the JET-ILW C38 He restart, with a minimum Lyman α intensity of 3.2×10^{20} ph (s·m^2·sr)$^{-1}$.

Table 5. Measured He Lyman series line intensity ratios at a Lyman α intensity of $\sim 3.5 \times 10^{20}$ ph (s·m^2·sr)$^{-1}$.

Campaign	JET-ILW (Restart)	JET-ILW (Experiment)
Pulses	93 023–93 089	93 847–93 908
KT7/2	Measured ratio	Measured ratio
α/β	5.65 ± 10%	5.25 ± 10%
β/γ	3.59 ± 10%	3.54 ± 10%
β/δ	9.38 ± 10%	8.92 ± 10%
β/ε	32.3 ± 10%	30.0 ± 10%
β/(fitted) ζ	69.5 ± 15%	67.3 ± 15%

The discrepancy for the Lyman β to ζ ratio arises because of the strong dependence of the Lyman β to ζ ratio on the Lyman intensity (figure 23).

3.4. Time histories of He II intensities in pulses demonstrating near-constant ratios

3.4.1. KT2 observations. The all pulse surveys presented in sections 3.1–3.3 show the frequency with which the near-constant ratios occur during operational periods. It is also instructive to follow the time dependence of line intensities during particular pulses. Figure 24 illustrates the time dependence of the Lyman α and β line intensities for a 2.25 T, 1.8 MA pulse, number 93 072, recorded with KT2 during the JET-ILW He restart. With a constant multiplication factor it can be seen how closely these line intensities follow each other during the low He intensity, equilibrium phase of the discharge. This pulse ends in a ragged MARFE-like termination, during which the rapidly changing intensities do not overlay and the ratios are no longer considered reliable.

Figure 25 shows time histories of the same lines for pulse 93 893 recorded during the JET-ILW He experiment. Again, the Lyman β intensity closely follows that of the Lyman α line despite numerous changes in intensity. These are due to a number of factors that would be expected to lead to changes in the plasma parameters, such as changes in gas puffing, both ICRH and NBI additional heating being applied and the plasma position changing, the plasma being moved closer to the inner wall at 16 s. The timings are illustrated in figure 26 which shows the time development of various plasma parameters. It is noted that sufficient smoothing of the time histories is applied in order to reduce the noise typical of these spectra and improve the reliability of the analysis. The smoothing used varies depending on the intensity of the observed line. Typically, a smoothing (using a boxcar average) over 5 scans is applied to the Lyman α and β lines. However, for weaker lines a smoothing of up to 35 scans can be used, for example, for the Lyman ζ line in the KT7/2 spectrum.

Pulse 78 908 is an example from the restart of the JET-C He campaign, the time histories of the Lyman α and β lines being shown in figure 27. This is a 2.1 T, 1.9 MA discharge. In this case the changes in the intensities are due to the use of up to 4.8 MW of He NBI. Before 6.5 s the spectrum is contaminated by C and a mismatch is also seen during the large He influx at the pulse termination during which the Lyman α intensity exceeds that of the Lyman β by more than an order of magnitude. However, throughout the rest of the pulse it is seen that the time histories, with a multiplication factor, can be overlaid.

3.4.2. KT7/2 observations. The higher spectral resolution of KT7/2 allows Lyman series line intensities up to the Lyman ζ line to be monitored and it is shown in figure 28 that the time

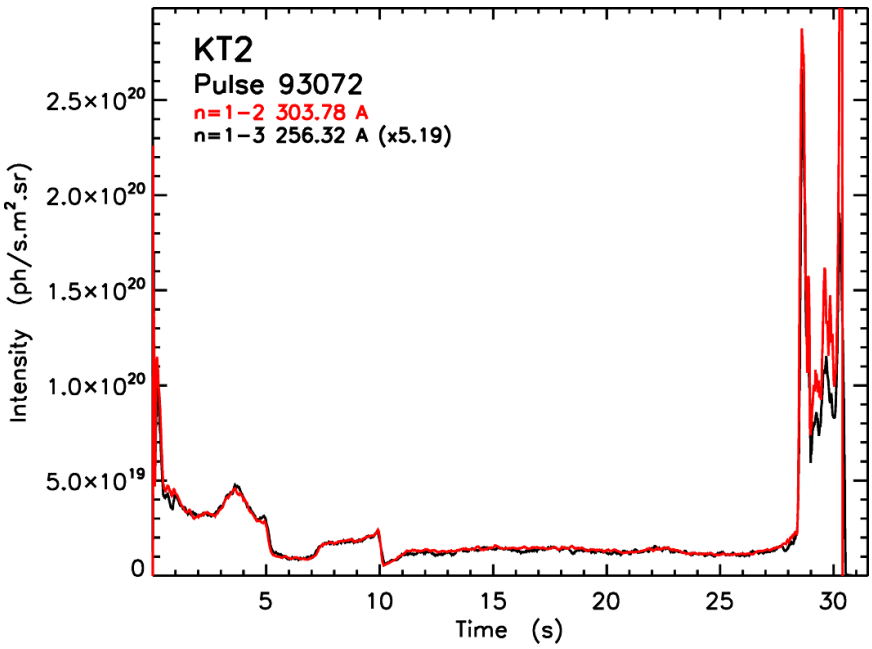

Figure 24. The Lyman α and β line intensities for pulse 93 072 recorded with KT2 during the JET-ILW C38 He restart.

histories of all the observed Lyman lines, with multiplication factors, can be overlaid for pulse 93 048. This pulse is a 2.2 T, 1.8 MA discharge run during the JET-ILW restart. It is necessary to carry out line fitting for the blended Lyman ζ line and this was only successful for some of the time points leading to a series of points being shown.

In a neighbouring pulse, number 93 051, a similar 2.2 T, 1.8 MA discharge, there was extreme detector saturation for the Lyman α line and some saturation seen for the Lyman β line as a result of different detector voltages being used. Figure 29 demonstrates that the line profiles can be successfully reconstructed, the time histories again largely overlaying. The spectrum with the most extreme saturation, recorded at 23.5 s, is illustrated in figure 30 where it is compared with an unsaturated spectrum at a time of 10.7 s. The algorithm searches for a previous unsaturated spectrum which is then used to reconstruct the saturated line profiles. It is noted that small differences in the reconstruction can result from the algorithm finding spectra with slightly differing line profiles (as is illustrated in figure 9). However, these differences are well within the expected errors quoted for the integrations.

Time histories of Lyman series line intensities measured with KT7/2 from the JET-ILW C38 He experiment and JET-C C27b campaign are shown in figures 31 and 32 for the same pulses whose KT2 data is displayed in figures 25 and 27, respectively. In figure 31 the time histories mainly overlay, with the exception of the Lyman ε line at 234.35 Å. This line is blended with the Ni XXVI line at 234.15 Å, whose intensity becomes significant during phases of ICRH and NBI additional heating (figure 26). Nevertheless, this demonstrates the advantage of using He discharges in this study where contaminants and blending such as this are minimized in comparison with D fuelled discharges. The blending of the Lyman ε line is worse in pulse 78 908 (figure 32) making this line unusable. Further there is blending of the Lyman δ line at 237.33 Å before 16 s with a Ni XVIII line at 236.33 Å and Ni XVI lines, the line profile being broadened by these blends. The most likely candidates for the latter are the Ni XVI lines at 237.49 Å and 237.86 Å.

3.5. Time histories of He II intensities in pulses deviating from near-constant ratios

3.5.1. KT2 observations. Pulse 93 075 is a 2.4 T, 1.4 MA Ohmic density limit pulse from the JET-ILW C38 He restart reaching a maximum density of 1.0×10^{20} m^{-3}. This results in intense He emission, the He Lyman α intensity observed by KT2 exceeding $\sim 7 \times 10^{19}$ ph (s·m^2·sr)$^{-1}$. The intensities can be seen in figure 33, which shows time histories of the first three Lyman series lines. The Lyman β and γ line intensities overlay, but fall short of the Lyman α intensity after $\sim$9.2 s. The Lyman γ intensity is obtained through line fitting and is therefore represented by a series of points.

In figure 34 corresponding traces are shown for pulse 93 899, which was run during the JET-ILW He experiment. A similar behaviour is observed to that seen in figure 33. The pulse is a 2.4 T, 1.9 MA discharge, studying the L- to H-mode transition in He. The large He influx at 13 s occurs when the NBI heating terminates, the time development of various plasma parameters being shown in figure 35.

Figure 36 illustrates a pulse from the JET-C C27b He campaign, pulse number 79 128. Only the Lyman α and β lines are shown in this diagram, since the Lyman γ line is blended. Again it can be seen that the former overlay during the low intensity equilibrium phase of the discharge, with the Lyman α to β ratio increasing when the He emission is high.

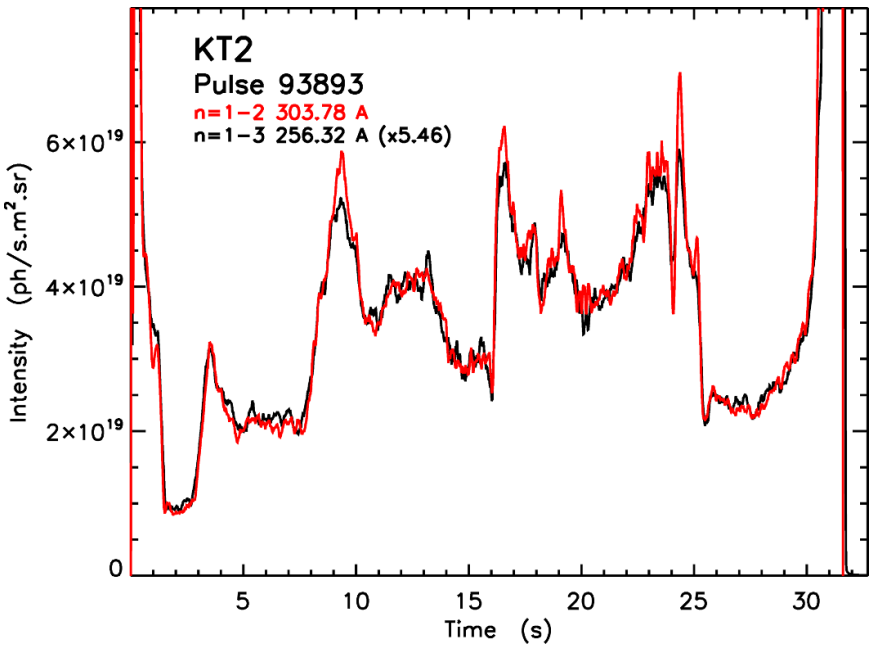

Figure 25. The Lyman α and β line intensities for pulse 93 893 recorded with KT2 during the JET-ILW C38 He experiment.

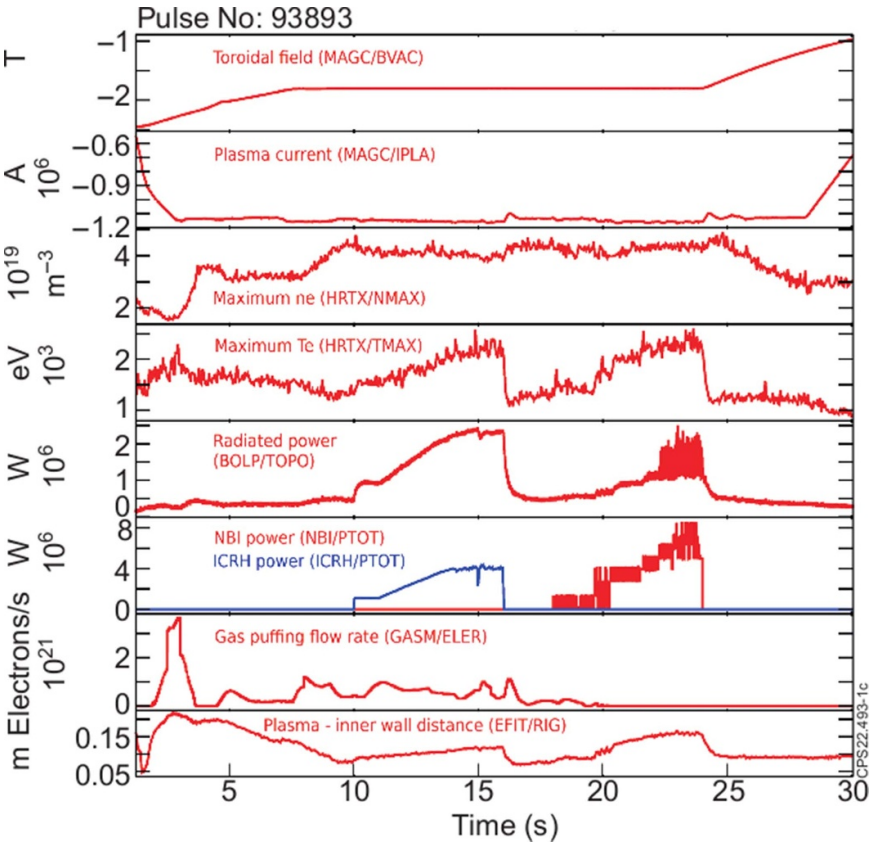

Figure 26. Plasma parameters for pulse 93 893.

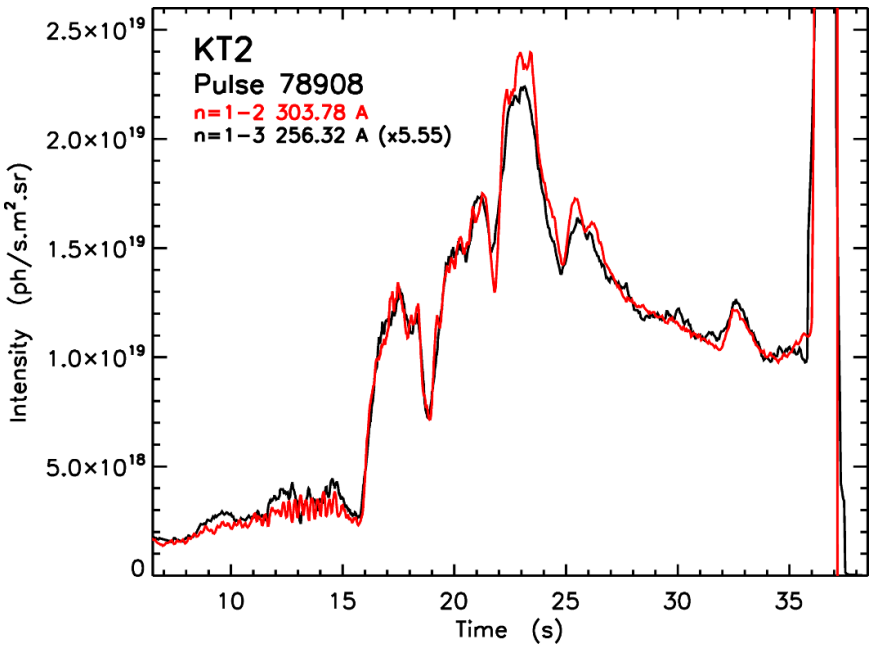

Figure 27. The Lyman α and β line intensities for pulse 78 908 recorded with KT2 during the JET-C C27b He campaign.

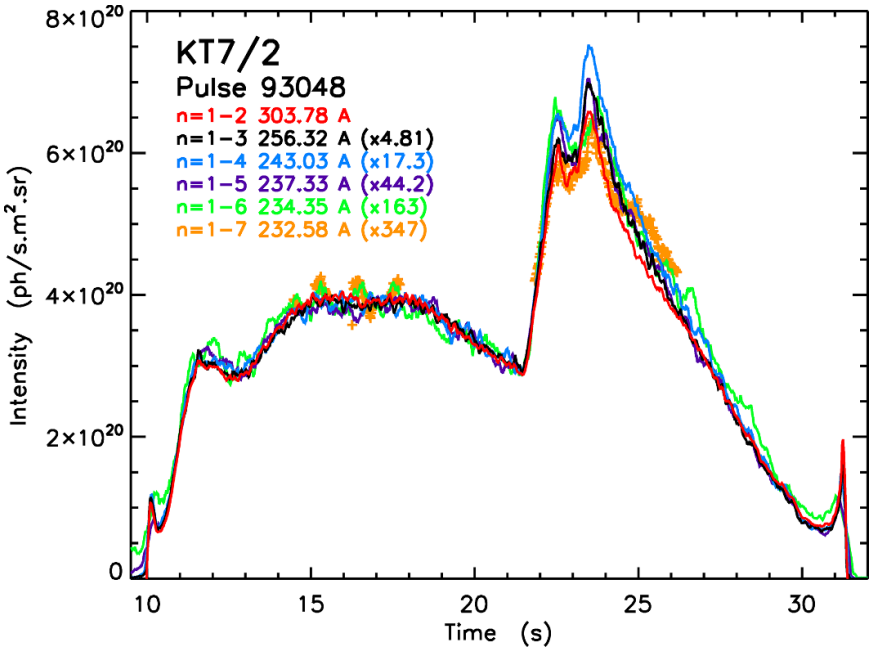

Figure 28. Lyman series line intensities for pulse 93 048 recorded with KT7/2 during the JET-ILW C38 He restart.

3.5.2. KT7/2 observations. The advantage of the higher resolution of KT7/2 is clearly seen in figure 37, which shows time histories of the Lyman series line intensities up to the Lyman ζ line for a 2.3 T, 1.8 MA Ohmic density ramp experiment, pulse number 93 056. This discharge was run during the JET-ILW He restart, during which no additional heating was available. After 16 s the line intensities can be seen to diverge with the higher members falling away from the Lyman α to γ intensities. Up to 23.3 s, the Lyman β and γ intensities overlay as is seen with the KT2 observations, after which the Lyman β to γ line ratio also increases. As before the Lyman ζ line intensity is obtained by line fitting and hence is shown by a series of points.

Figure 38 shows time histories of the KT7/2 measurements for pulse 93 899, the same pulse used to illustrate the KT2 time histories in figure 34. The plasma parameters for this pulse are illustrated in figure 35. The significant rise in the He emission at 13 s observed by KT2 along a horizontal line-of-sight is matched by a sharp fall in the divertor emission. In this pulse low levels of Cu are present, which affect both the Lyman ε

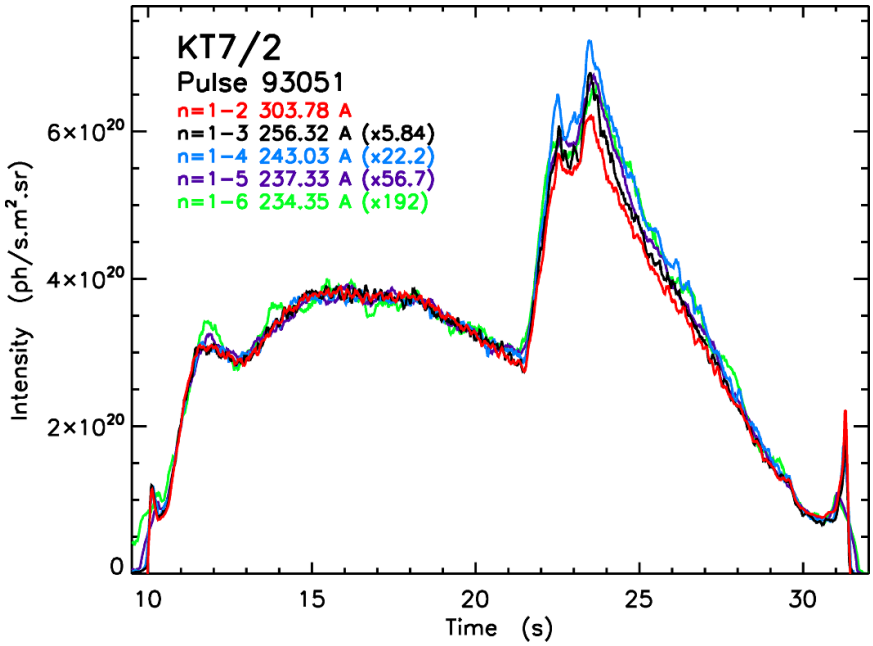

Figure 29. Lyman series line intensities for pulse 93 051 recorded with KT7/2 during the JET-ILW C38 He restart, a pulse in which there is heavy detector saturation.

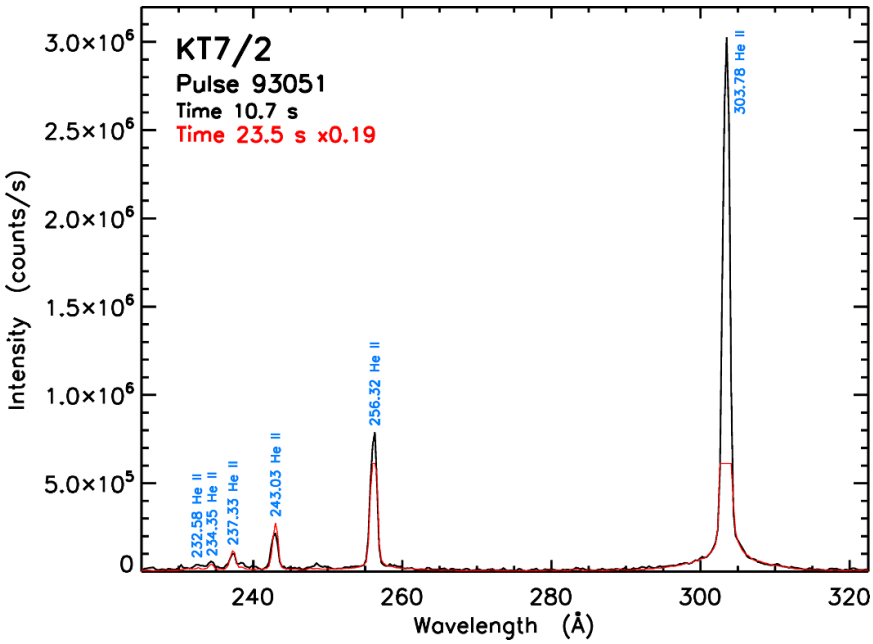

Figure 30. The spectrum of pulse 93 051 recorded with KT7/2 showing the extreme saturation of the detector in the Lyman α line at time 23.5 s compared with an unsaturated spectrum at 10.7 s.

and β lines in the KT7/2 spectrum. The Lyman ε line is blended with the intense Cu XVIII line at 234.20 Å and when the Cu line intensities are highest the Lyman β line is affected by weak Cu XVIII lines at 256.21 and 256.61 Å.

An example of a discharge with intense He emission from the C27b campaign is a 2.3 T, 2.4 MA Ohmic density limit pulse number 79 205 (figure 39) which reaches a density of 7.0×10^{19} m^{-3}. The Lyman series line intensities overlay during the low intensity phase of the discharge, but diverge after 17 s as the density and hence He emission increases.

3.6. Time histories of He II intensities viewed along different lines-of-sight

The observations presented above have been recorded along three different lines-of-sight, one horizontal and two along vertical views into the divertor. It is of interest to check two other lines-of-sight for which data is available. For the earlier JET-ILW campaigns, from C28 up until the end of C36b (August 2011–November 2016), KT7 was usually aligned to view the outer divertor throat. For a limited period (25

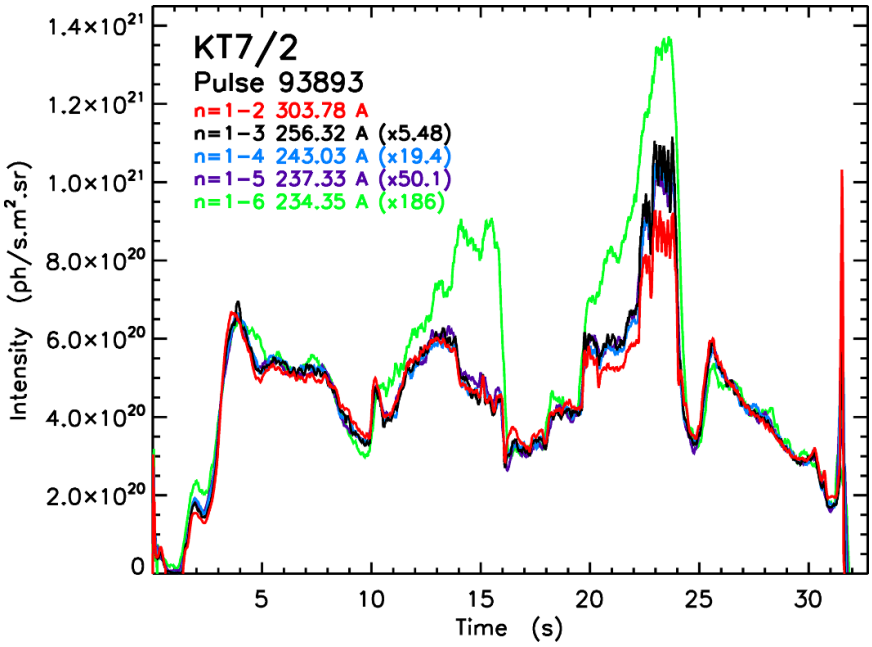

Figure 31. Lyman series line intensities for pulse 93 893 recorded with KT7/2 during the JET-ILW C38 He experiment. The Lyman ε line at 234.35 Å is blended with the Ni XXVI line at 234.15 Å.

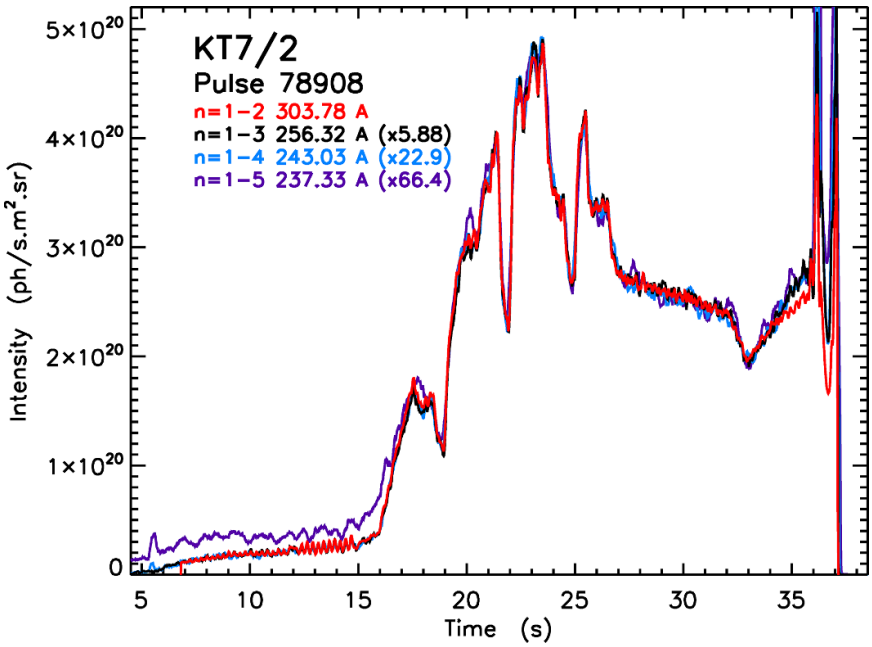

Figure 32. Lyman series line intensities for pulse 78 908 recorded with KT7/2 during the JET-C C27b He campaign. The Lyman δ line at 237.33 Å is blended with Ni XVI and Ni XVIII lines before 16 s.

August to the 8 October 2016) during the C37 H campaign and the following restart to the C36b campaign, KT7 had a more central view of the divertor than in the later C38 or C27b campaigns, the latter with its view to the inner divertor target plate. These additional lines-of-sight are shown in figure 40.

Two pulses studying the isotope dependence of the L-H transition are chosen from the C37 H campaign. Pulse 91 445 is a 3.1 T, 2.6 MA discharge, with 7.4 MW of H NBI, together with 6.8 MW of He^3 minority ICRH. The KT7 view is towards the outer divertor throat. Two He gas puffs were used during this pulse; the first from 8.0–8.2 s had a flow rate of 1.9×10^{21} electrons·s^{-1}, the second from 9.0–9.76 s a flow rate of 7.9×10^{20} electrons·s^{-1}. The high toroidal field meant that an L-H transition was not achieved, the pulse ending in a density limit disruption after it reached a peak density of

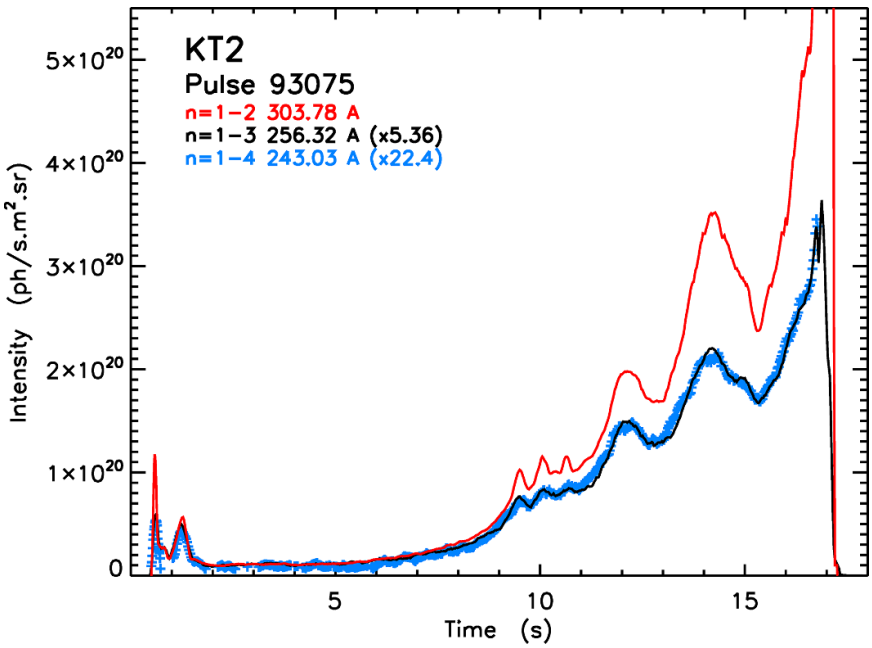

Figure 33. The Lyman series line intensities for pulse 93 075 recorded with KT2 during the JET-ILW C38 He restart.

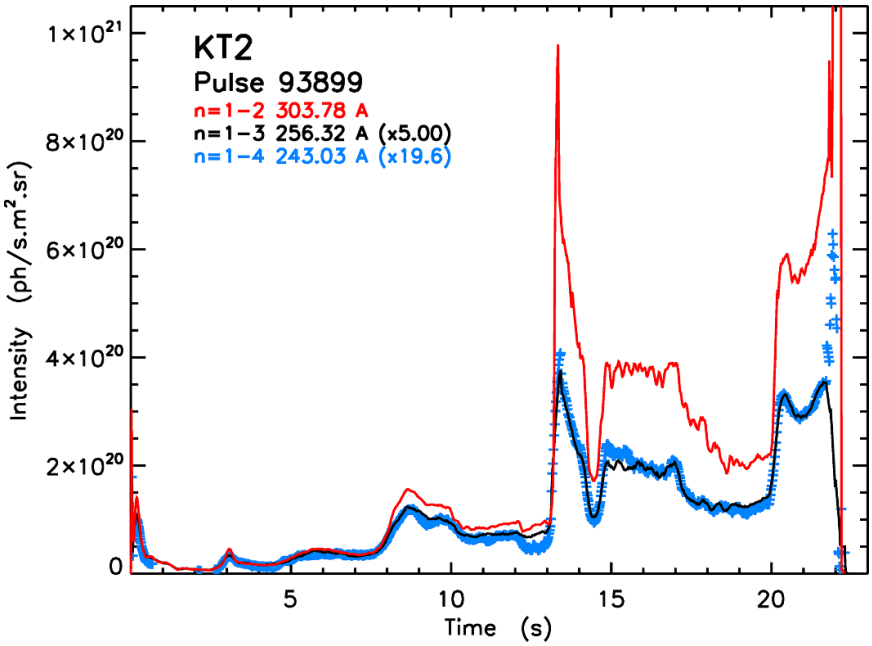

Figure 34. The Lyman series line intensities for pulse 93 899 recorded with KT2 during the JET-ILW C38 He experiment.

7.8×10^{19} m^{-3}. Figure 41 shows the time development of the Lyman series line intensities. With this view emission from the plasma core is becoming relatively more important than in the earlier cases illustrated. The 234.35 Å He II line is blended with the intense 234.15 Å, Ni XXVI and the 234.20 Å, Cu XVIII lines. The 237.33 Å He II line is also blended with a Ni XVI transition at 237.49 Å. Even the 243.03 Å, He II line shows some evidence of blending, the most likely candidates in this case being weak Cr or Fe lines or even an Ar XIV line at 243.75 Å, since residual Ar is seen in the plasma.

Pulse 91 728 was run during the period when KT7 had the more central view of the divertor. The discharge has a toroidal field of 1.8 T and plasma current of 1.6 MA. A He gas puff starts at 9 s rising to a flow rate of 8.3×10^{20} electrons·s^{-1} by 11 s. This leads to ∼15% concentration of He in the plasma. H NBI starts at 10 s rising in steps to 6.0 MW with an L-H transition ocurring at 12.2 s. Again the pulse ends in a density limit disruption with a maximum density of 7.0×10^{19} m^{-3}. The time histories of the Lyman series line intensities are shown in figure 42. The 234.35 Å He II line is blended, but

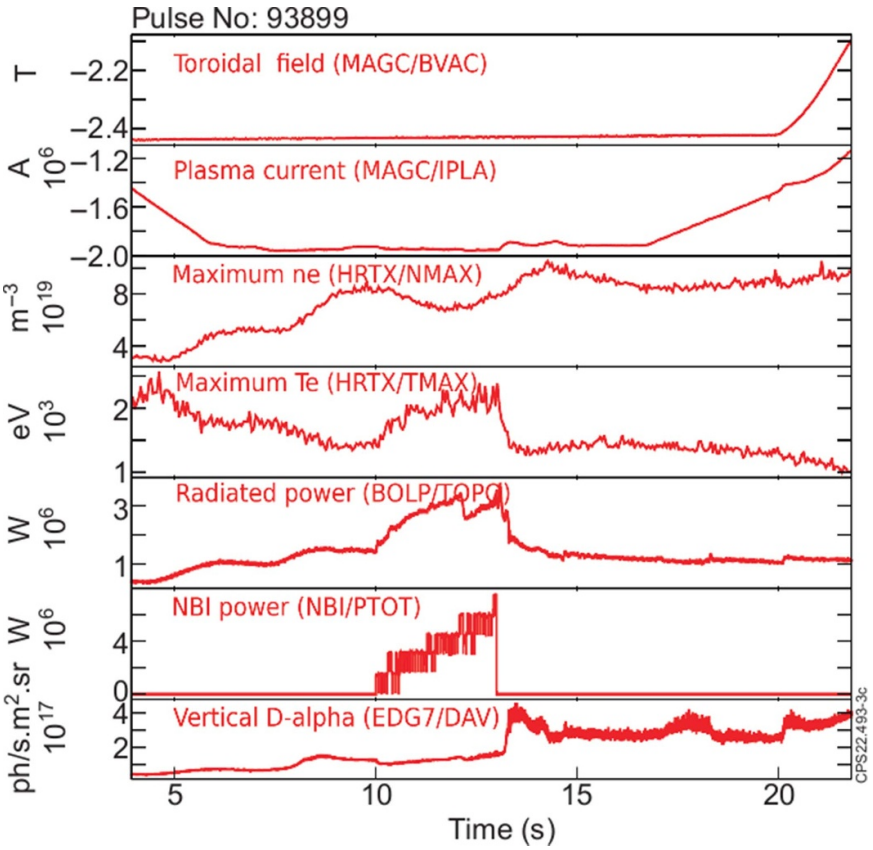

Figure 35. Plasma parameters for pulse 93 899.

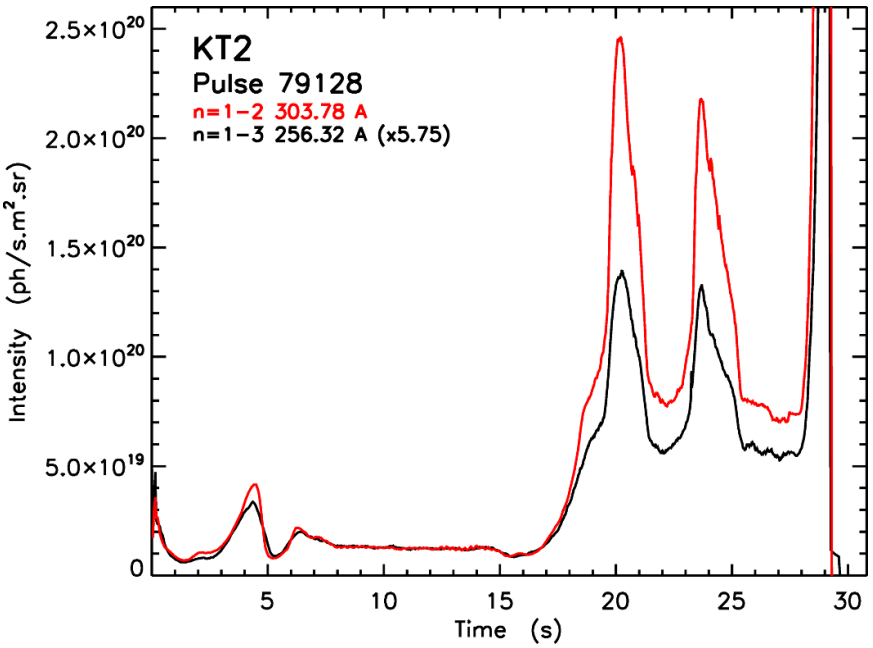

Figure 36. Lyman α and β line intensities for pulse 79 128 recorded with KT2 during the JET-C C27b He campaign.

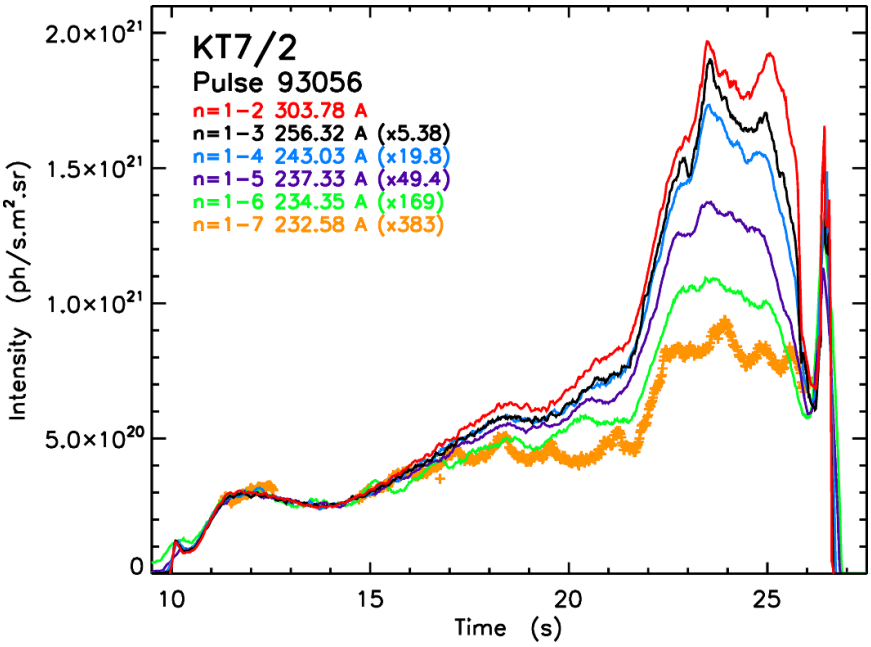

Figure 37. The Lyman series line intensities for pulse 93 056 recorded with KT7/2 during the JET-ILW C38 He restart.

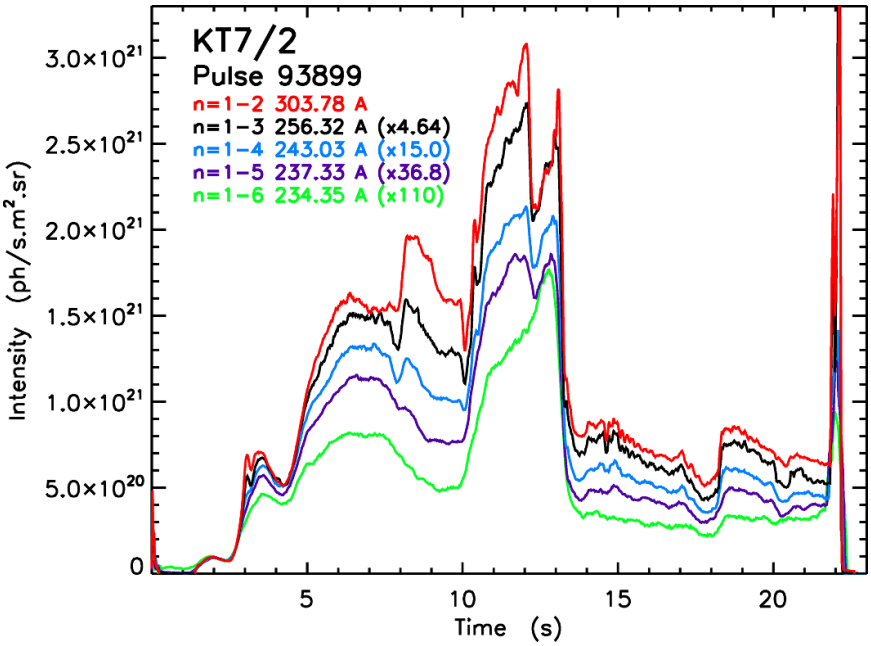

Figure 38. The Lyman series line intensities for pulse 93 899 recorded with KT7/2 during the JET-ILW C38 He experiment.

only with the 234.15 Å, Ni XXVI line, Cu being less important in this discharge. The Lyman α, β and γ lines saturate towards the end of the pulse and corrections to all three lines were applied. It can be seen that the Lyman α line falls below the trajectory of the Lyman β and γ lines, which is thought due to opacity. In both these pulses, the Lyman series line intensity ratios during the equilibrium phase of the pulse are, within errors, the same as is seen with the other lines-of-sight. This provides further confirmation that the measured Lyman series ratios do not depend on the line-of-sight and suggests a localized region of emission.

3.7. Observations made by the poloidally scanning VUV spectrometer

Since the results presented above are all made with SPRED spectrometers the survey of the VUV Lyman series is completed with observations from KT1, a poloidally scanning spectrometer. KT1 employs a different spectrometer mount and different detectors, therefore avoiding any concern of bias due to possible instrumental effects. The spectrometer is able to record measurements of two spectral lines, although as explained in section 2, with a limitation that the lines must be

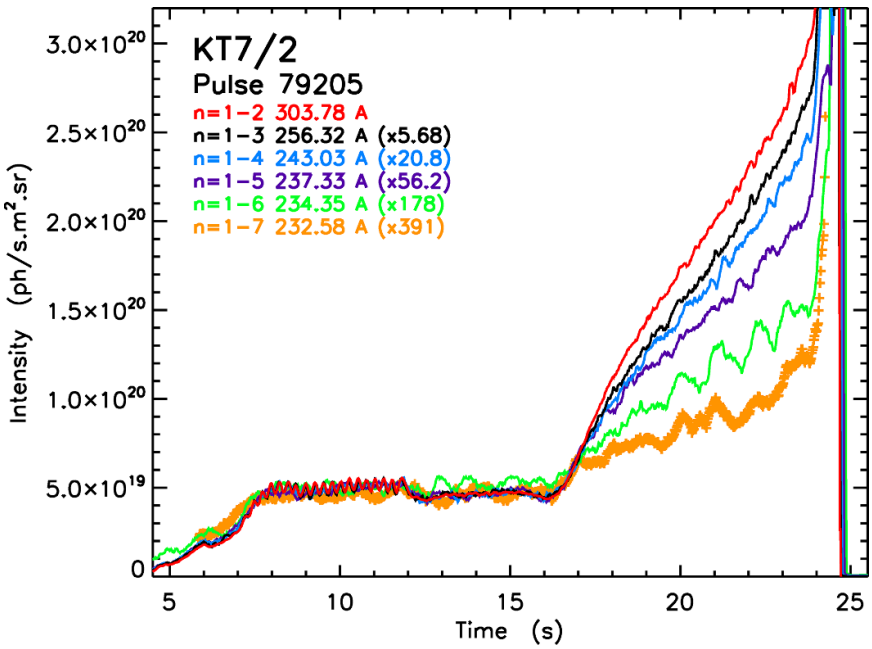

Figure 39. The Lyman series line intensities for pulse 79 205 recorded with KT7/2 during the JET-C C27b He campaign.

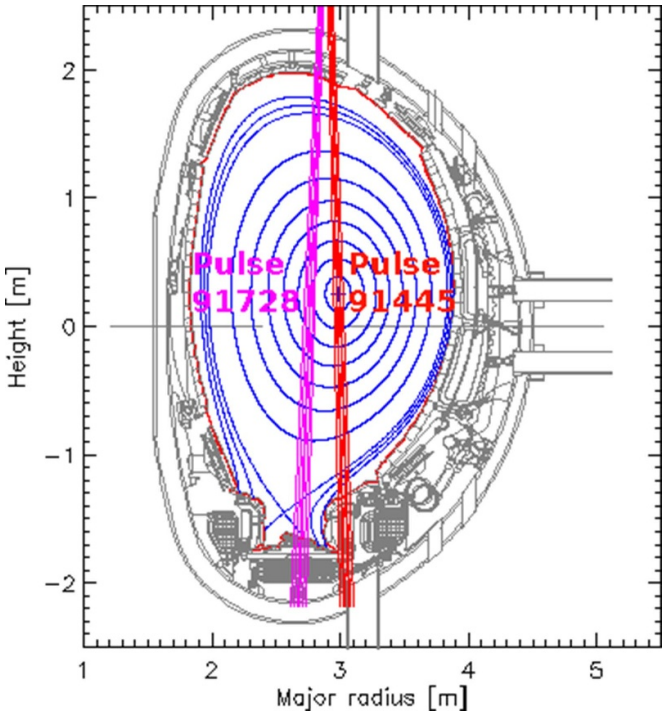

Figure 40. Lines-of-sight of the KT7 VUV spectrometer for pulses 91 445 and 91 728, together with the magnetic configuration at 15 s in pulse 91 728.

well separated due to the physical size of the detectors. At short wavelengths around those of the He II Lyman series the minimum separation of the detectors is ∼190 Å. Consequently, the Lyman series data must be recorded in different pulses.

Pulses 90 379, 90 381 and 90 383 are part of a series of similar discharges run during the JET-ILW C36 campaign in April 2016. Although D fuel was used in these 2.1 T, 2.0 MA, ELMy H-mode pulses, He^4 was gas-puffed in order to study its effect on confinement. The short wavelength detectors on KT1 were set to record, respectively, the Lyman α, β and γ lines. The poloidal profiles across the divertor at three times, 8.5, 8.8 and 9.0 s, are shown in figures 43–45, respectively. It should be recognized that these pulses are not identical and that allowance for somewhat different He levels has been made using the Lyman α measurements of KT7/2. Nevertheless, there are clear similarities between the profiles, with a development from 8.5 s when the He intensities were comparatively low to higher densities and, consequently, higher He intensities after 12 MW of D NBI additional heating was applied from 8.5 s. Again, the measured Lyman series line intensity ratios are similar to those recorded with KT2 and KT7/2 confirming that the measured ratios do not depend on the line-of-sight or are a feature of the SPRED spectrometers. In these pulses there is further evidence of the Lyman α line being affected by opacity during the peak He emission. In figure 45 the intense emission observed in the outer divertor in pulses 90 379 and 90 383 is due to ELMs.

4. Comparisons with higher He series members

In the hydrogen-like species occurring in tokamak plasmas most of the population of the electron energy levels is in the ground state. Hence Lyman radiation, whose transitions end in the ground state, is absorbed as it travels towards the observing instrument. The rapid re-emission of the radiation is isotropic meaning that the spectrometers, especially those with the small acceptance angles typical of VUV instruments, will not see the re-emitted photons. This raises the question as to the reliability of the VUV observations in the high density ($>10^{20}$ m^{-3}), low temperature (<4 eV) regimes expected in divertor plasmas in

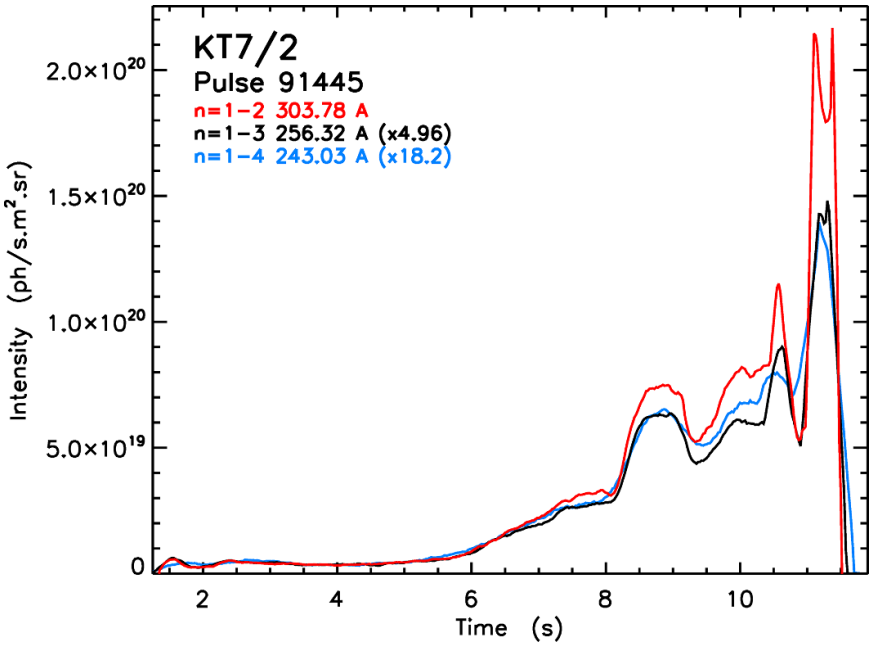

Figure 41. The Lyman series line intensities for pulse 91 445 recorded with KT7/2 during the JET-ILW C37 H campaign. The line-of-sight is towards the outer divertor throat.

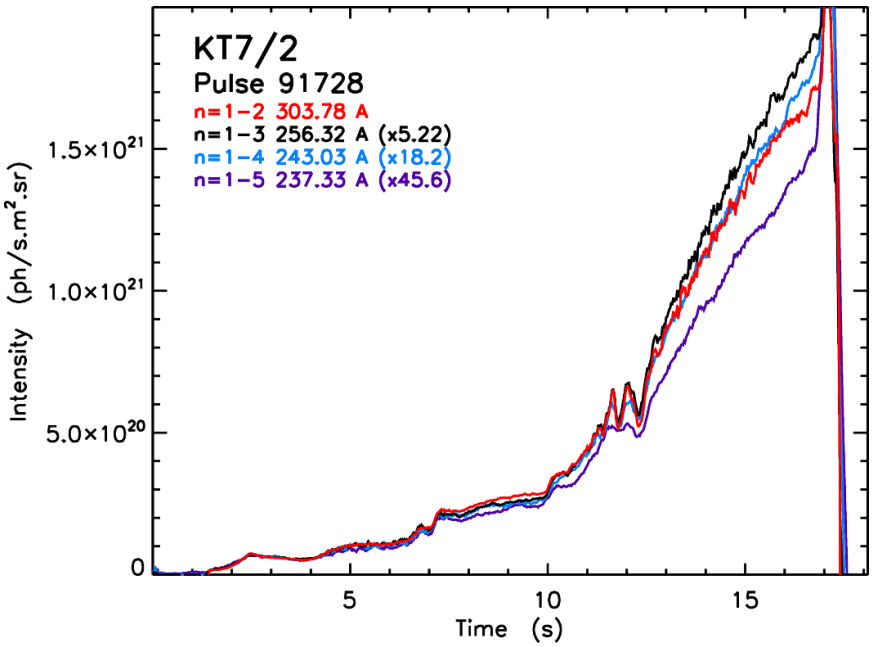

Figure 42. The Lyman series line intensities for pulse 91 728 recorded with KT7/2 during the JET-ILW C37 H campaign. The divertor view is more central than in the C38 campaign.

which the opacity may be extreme. Comparisons with higher He series members, which are not affected by opacity, are therefore used to judge how serious is the loss of intensity due to opacity in the Lyman series lines.

The most direct comparisons are those made between spectral lines having the same upper levels. These are called 'branching ratios'; the line intensity ratios are determined solely by the A values. In most observations of hydrogen-like species, as in the present case, the components of the lines are not spectrally resolved. These are not true branching ratios, since there are only two allowed components of the Lyman series lines, the 1 s $^2S_{1/2}-n$p $^2P_{1/2,3/2}$ transitions, whereas a number of allowed transitions are possible between the higher series members. Consequently, the ratio between the Lyman and higher series line intensities must be modelled to see to what extent they differ from the ratio of the averaged transition probabilities for the unresolved lines determined assuming statistical populations of the energy levels within a shell.

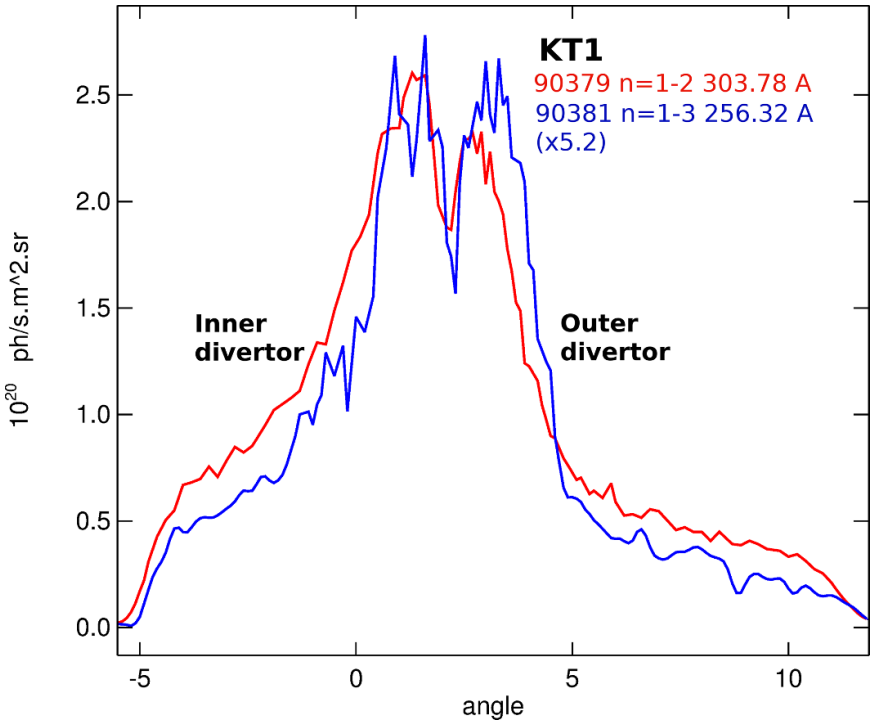

Figure 43. Poloidal profiles of the Lyman α and β line intensities for pulses 90 379 and 90 381 recorded at 8.5 s with the vertical KT1 system during the JET-ILW C36 D campaign.

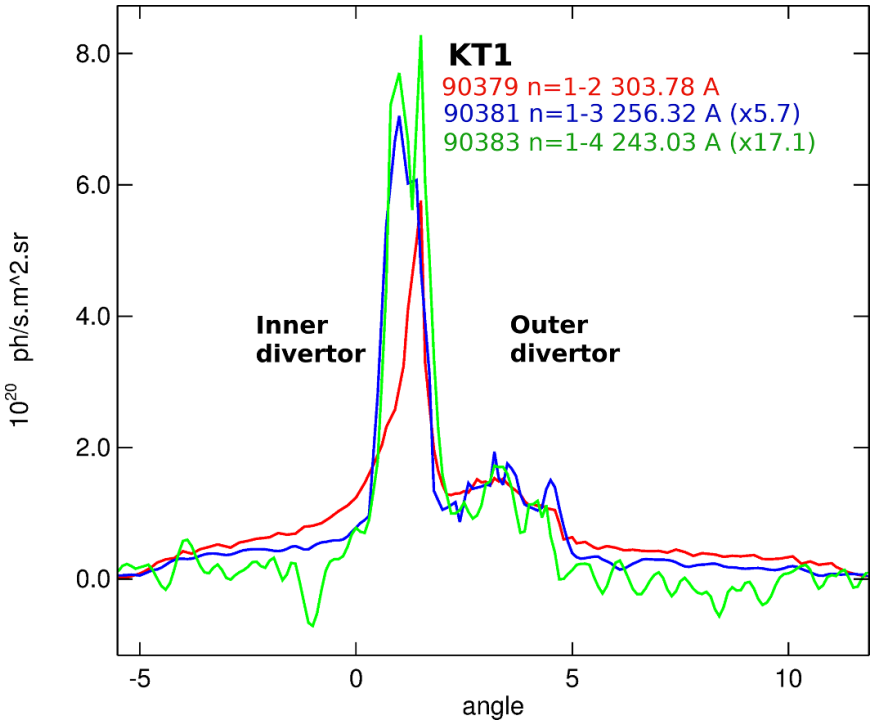

Figure 44. Poloidal profiles of the Lyman series line intensities for pulses 90 379, 90 381and 90 383 recorded at 8.8 s with the vertical KT1 system during the JET-ILW C36 D campaign.

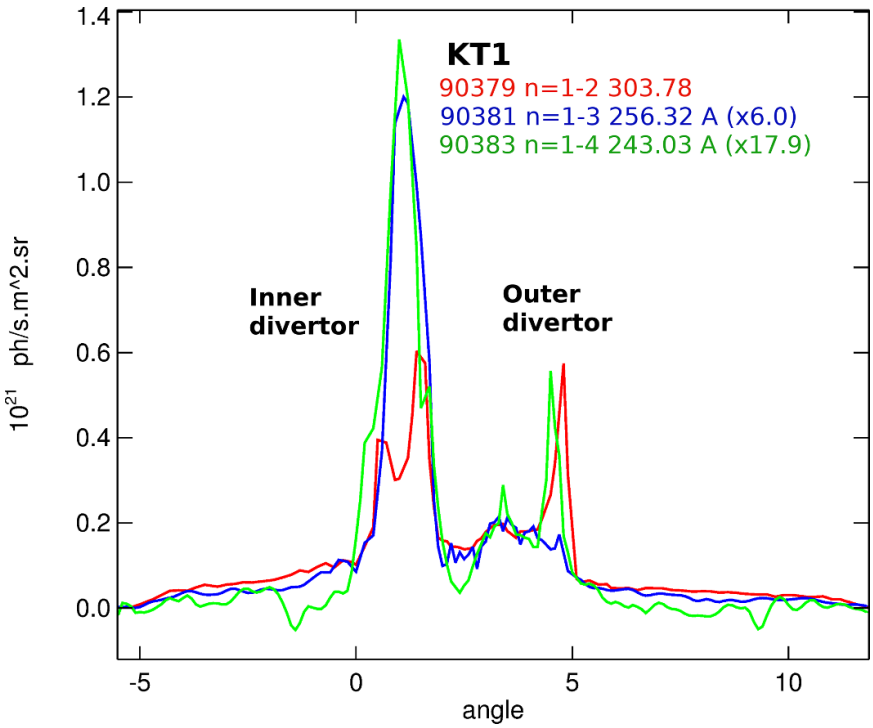

Figure 45. Poloidal profiles of the Lyman series line intensities for pulses 90 379, 90 381and 90 383 recorded at 9.0 s with the vertical KT1 system during the JET-ILW C36 D campaign. The Lyman α line shows evidence of opacity.

Table 6 lists the various line combinations of He II which have the same upper levels and it can be seen that there are only two that are useful for these measurements on JET.

The most accurate measurements of line intensity ratios are obtained when the same spectrometer observes both lines. However, comparisons between different series members of a hydrogen-like species are often complicated by higher spectral orders of the short wavelength line blending with the first spectral order of the longer wavelength higher series member. In many cases, the higher spectral orders can be intense enough to mask the first order emission. This is the case with the $n = 2$–4 transition, where even the 4th order of the intense 303.78 Å line makes the measurement of the $n = 2$–4 line unreliable. Consequently, the only VUV line that can be observed with the same spectrometer as a Lyman series line is the $n = 2$–5, Balmer γ line, which is very weak.

Nevertheless, the use of the same spectrometer overcomes a difficulty experienced when different instruments are used in that it ensures that exactly the same plasma is viewed for both lines. The difference in the viewing (acceptance) angles, particularly of VUV and visible spectrometers, means that a reliable comparison is only possible between these instruments when the spatial variation of parameters such as fuel and impurity densities and temperatures throughout the viewing geometry is small. When viewing the JET divertor, where these parameters vary rapidly, a comparison is only possible if poloidally scanning instruments are used. Consequently, comparisons between VUV and visible spectrometers with single lines-of-sight are most reliable when measurements are made along a horizontal view towards the main plasma. The ratio of the $n = 1$–4, VUV Lyman γ and $n = 3$–4, Paschen α lines is an example, with the latter falling in the visible spectral region.

4.1. Theoretical 'branching ratios'

Table 6 lists the averaged 'branching ratios' derived assuming the energy levels within a shell are statistically populated. These apply to the high density limit when collisions ensure that a statistical population is achieved. The deviation from these values for the line pairs that can be used on JET are shown in figures 46 and 47. It can be seen that differences from the high density limit are small for the parameter range of interest, comparable to or less than the expected experimental errors; they only become significant at densities less than 10^{19} m^{-3}.

4.2. The Lyman γ to Paschen α line intensity ratio

The Lyman γ to Paschen α line intensity ratio is obtained from two different spectrometers, one covering the VUV spectral region, the other a visible spectrometer. On JET it is necessary to use single line-of-sight instruments for these measurements, the difference in their acceptance angles meaning that the most reliable measurements are those that view the main chamber plasma along a horizontal line-of-sight. For the present measurements, both instruments used view the plasma along an 18 m long beamline so that the issue of viewing angles should be less important. Although this might be expected to ensure that both instruments view the same plasma, there is nevertheless a large spread in the data, $\sim\pm33\%$, which cannot be

Table 6. Comparison lines between the He II Lyman and higher series members.

Transition	Series	Wavelength (Å)	Averaged 'Branching ratio'	Comment
$n = 1$–3	Lyman β	256.32		VUV
$n = 2$–3	Balmer α	1640.4	1.264	Not observed on JET
$n = 1$–4	Lyman γ	243.03		VUV
$n = 2$–4	Balmer β	1215.1	1.519	Blend with 4th O of 303.78 Å
$n = 3$–4	Paschen α	4685.8	1.423	Visible
$n = 1$–5	Lyman δ	237.33		VUV
$n = 2$–5	Balmer γ	1084.9	1.630	Very weak VUV
$n = 3$–5	Paschen β	3203.1	1.874	Not observed on JET
$n = 4$–5	Brackett α	10 123	1.528	Not observed on JET

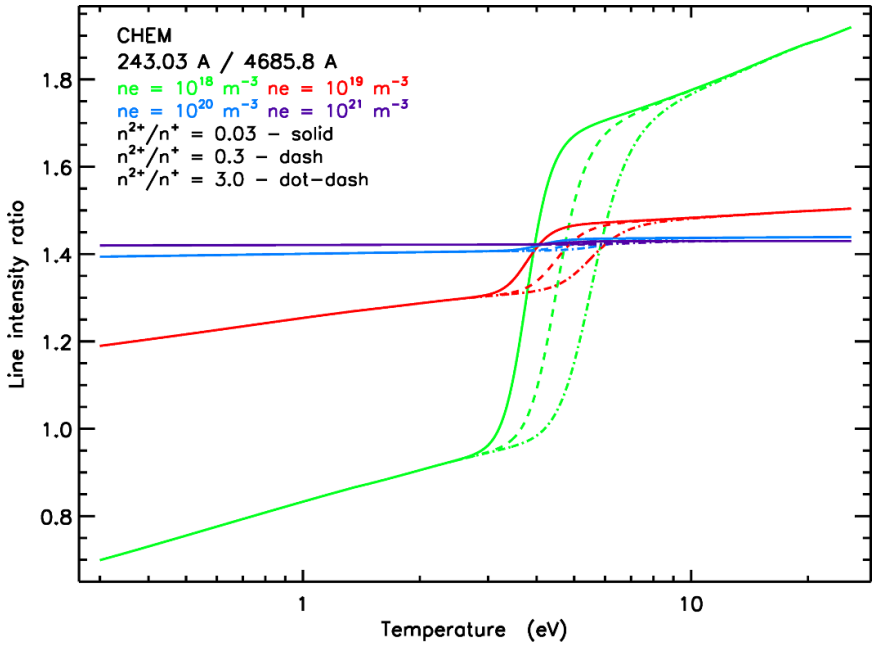

Figure 46. Theoretical He II Lyman γ to Paschen α line intensity ratio.

explained by the measurement errors alone. The KT2 spectrometer is used for the VUV measurement and spectral line profile fitting is needed to obtain the Lyman γ intensity, for which the accuracy is expected to be better than $\pm$15%. In the analysis, a minimum intensity is used for the visible Paschen α line at 4685.8 Å measured with the KS3/KSRA spectrometer ensuring that this line is clearly seen with a higher measurement accuracy of $\sim\pm$5%.

The Lyman γ to Paschen α intensity ratios are shown in figures 48 and 49 for the JET-ILW C38 restart and experiment, respectively, the intensities as before being averaged over 0.5 s intervals. The KS3 spectrometers were calibrated before the C38 campaign using an in-vessel calibration light source (Conway *et al* 2018) and a comparison of the absolute intensities of the 5270.6 Å Be II line observed with two different KS3 instruments with similar horizontal views confirms the validity of the calibrations for the He restart. However, by the time of the He experiment in June 2019 the calibration had changed, the sensitivity increasing by 32% from that of the He restart. Abrupt changes, which may be increases or decreases, are not unusual with either VUV or visible spectrometers. In many cases they can be related to a particular event, such as a plasma disruption, and are most likely due to small shifts in the line-of-sight of the instrument. The comparison between the VUV KT2 and visible KS3 instruments allows the VUV absolute sensitivity calibration to be checked and this was corrected in order to match the theoretical branching ratio. The ratio for the high density limit is shown in figures 48 and 49.

In figures 48, 12 points have been removed because an inspection of the spectrum showed that the Lyman γ line was affected by line blending and 1 point because the ratio was regarded as being unreliable due to the data being recorded during the termination of the pulse. During the He experiment a wider range of plasma parameters was used together with additional heating meaning that, with increased impurity levels, the blending was more severe. Consequently 24 points have been removed from figure 49 because of blending. There were also more points affected by the plasma termination leading to a further 44 points being excluded from this figure. In all of the latter cases the ratio was found to be higher than the general trend of points. In both periods of operation, two pulses are seen to be exceptional again with higher

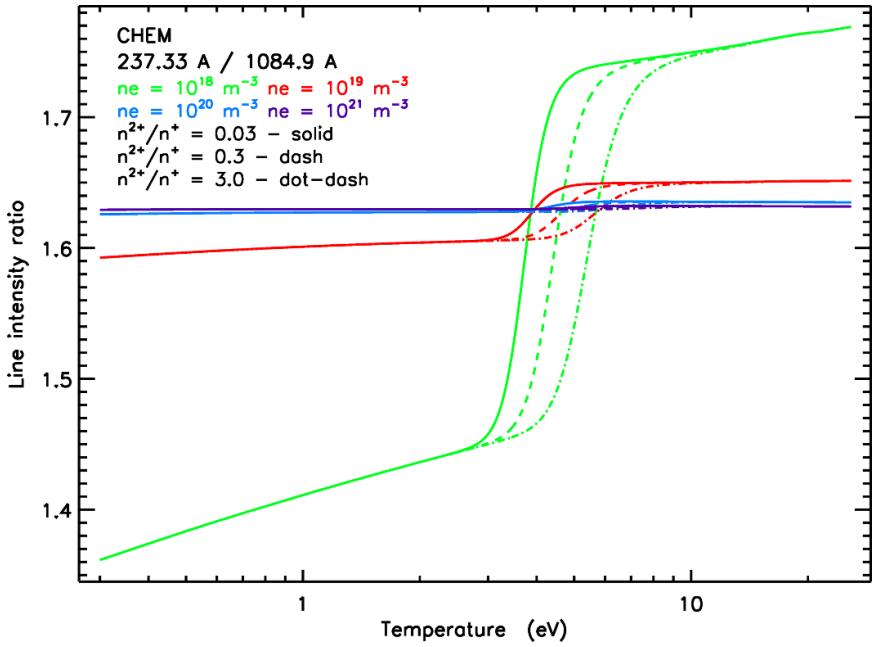

Figure 47. Theoretical He II Lyman δ to Balmer γ line intensity ratio.

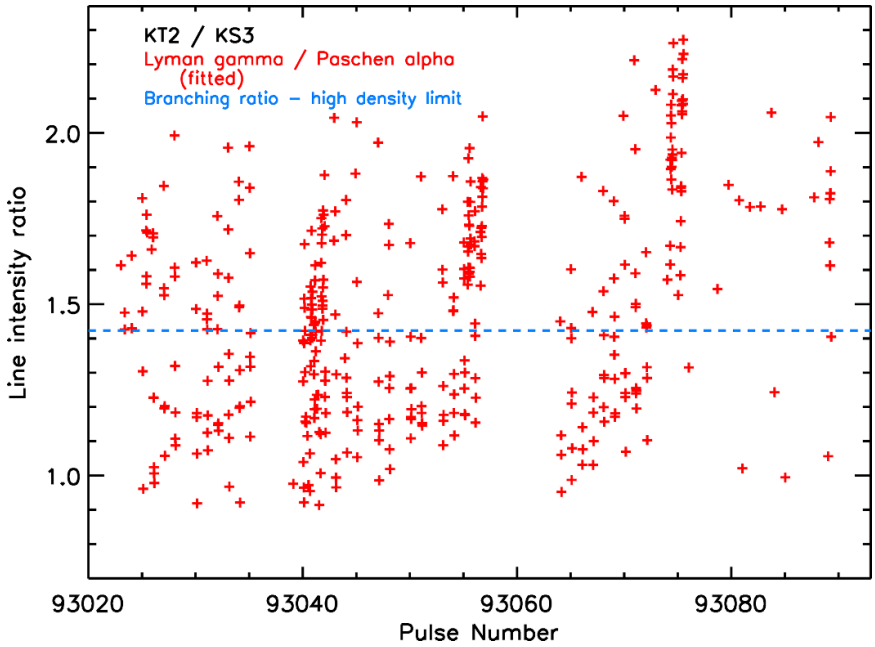

Figure 48. He II Lyman γ to Paschen α line intensity ratio measured during the JET-ILW C38 He restart. The Paschen α data at 4685.8 Å has a minimum intensity of 1.5×10^{17} ph $(\mathrm{s{\cdot}m^2{\cdot}sr})^{-1}$.

ratios. In figure 48, pulses 93 074 and 93 075 include a density ramp. In figure 49, pulses 93 899 and 93 900 have a particularly high density at the time of the excursion from the bulk of the dataset.

In neither the He restart nor experiment are any points found which lie below a ratio of ∼0.8. Such points would correspond to a significant Paschen α intensity together with an exceptionally low Lyman intensity. This could cast doubt on the reliability of the Lyman measurement.

4.3. The Lyman δ to Balmer γ line intensity ratio

The other possible check is of the Lyman δ to Balmer γ line intensity ratio. Both lines fall in the wavelength range of the KT7/1 survey spectrometer, although it must be recognized that the Balmer γ line is very weak, this being a limitation of the present measurements. A further complication arises in that the KT7/1 spectrometer has a similar spectral resolution to KT2, ∼5 Å, the Lyman δ line forming part of a blend of the higher Lyman series members. Although the intensity of

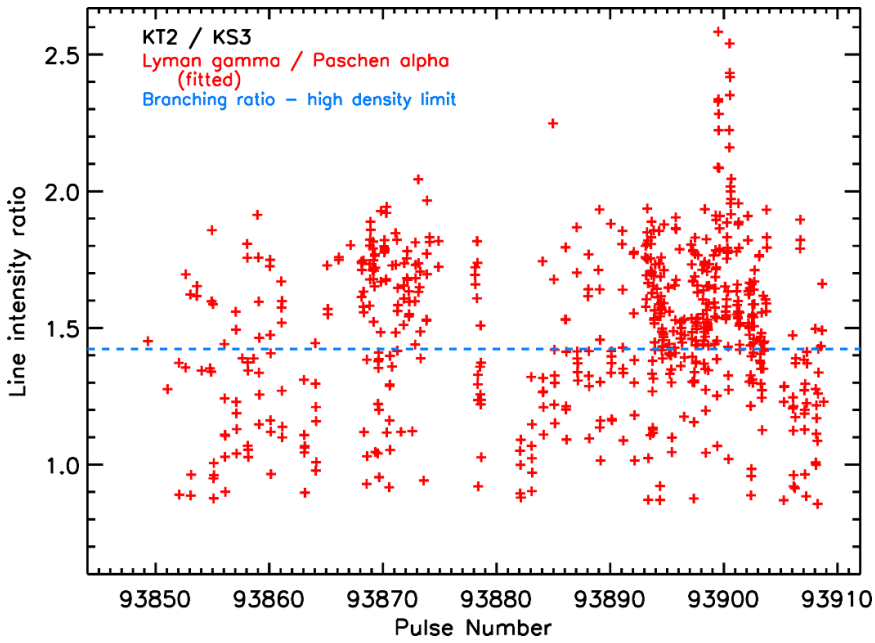

Figure 49. He II Lyman γ to Paschen α line intensity ratio measured during the JET-ILW C38 He experiment. The Paschen α data at 4685.8 Å has a minimum intensity of 1.8×10^{17} ph $(\mathrm{s{\cdot}m^2{\cdot}sr})^{-1}$.

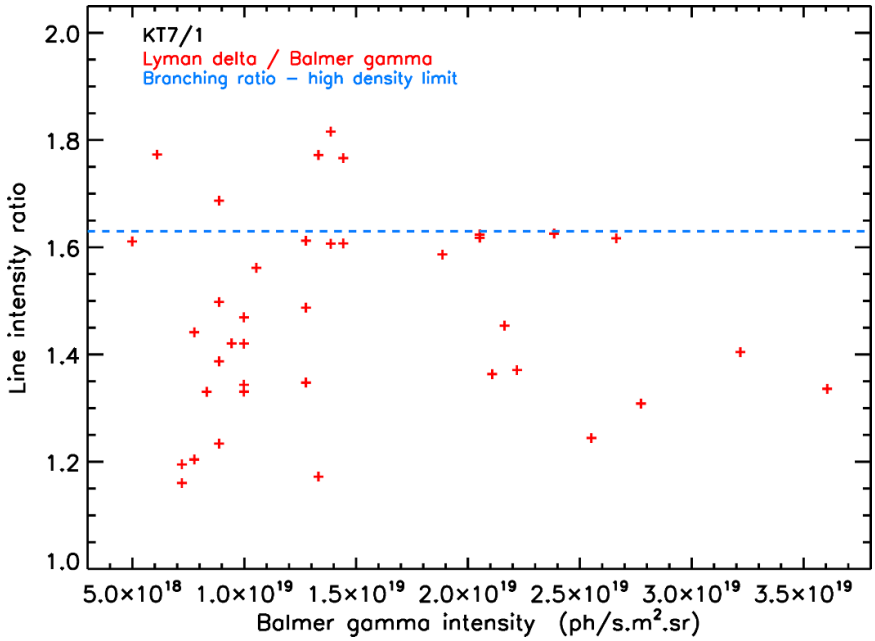

Figure 50. He II Lyman δ to Balmer γ line intensity ratio against the Balmer γ line intensity measured during the JET-ILW C38 He restart and experiment.

the Lyman γ line at 243.03 Å can be obtained by line profile fitting, the Lyman δ line at 237.33 Å cannot either be resolved by itself or its intensity determined reliably by line fitting. Nevertheless, it can be observed unblended in the second spectral order and since it is only necessary to determine whether the Balmer γ line can be observed without the Lyman δ line being seen, the analysis used the second order observation.

A search has been made of the two periods of JET-ILW C38 pulses in which He was used as the fuel. Time histories of the two lines are compared and matched when the intensity of the Balmer γ line at 1084.9 Å is highest, a visual check of the spectral line profile of both lines being carried out. Any evidence of the weak 1084.9 Å line being affected by neighbouring lines led to the measurement being rejected. The calibration for the second order spectrum of the 237.33 Å line is obtained by comparing the first and second order spectra of the neighbouring 256.32 and 243.03 Å lines and extrapolating to the Lyman δ line at 237.33 Å. As in the KT2 spectrum the intensity of the first order 243.03 Å line can be reliably obtained by line fitting.

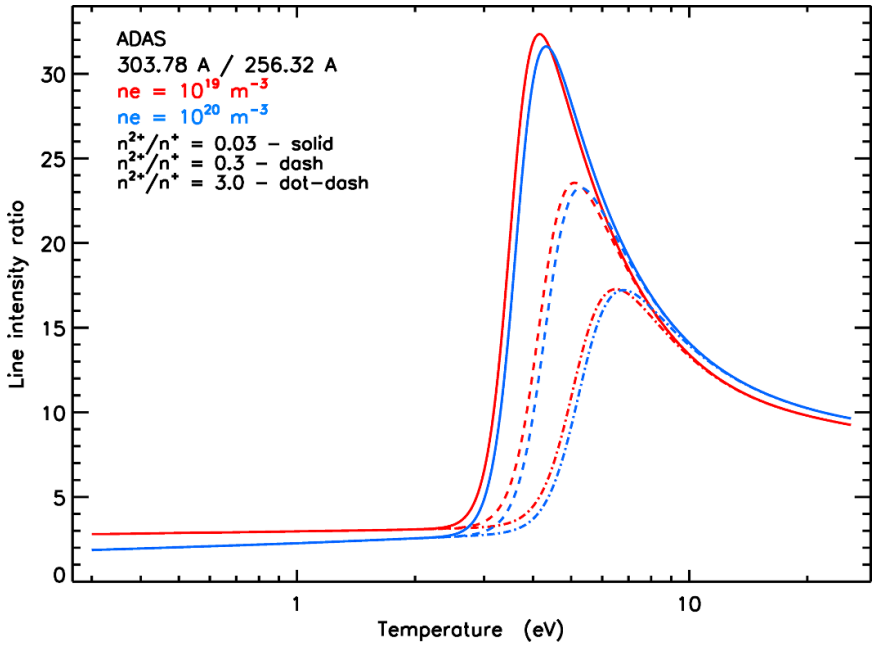

Figure 51. ADAS Lyman α to β line intensity ratios for two electron densities and three fully stripped He to He II ion density ratios.

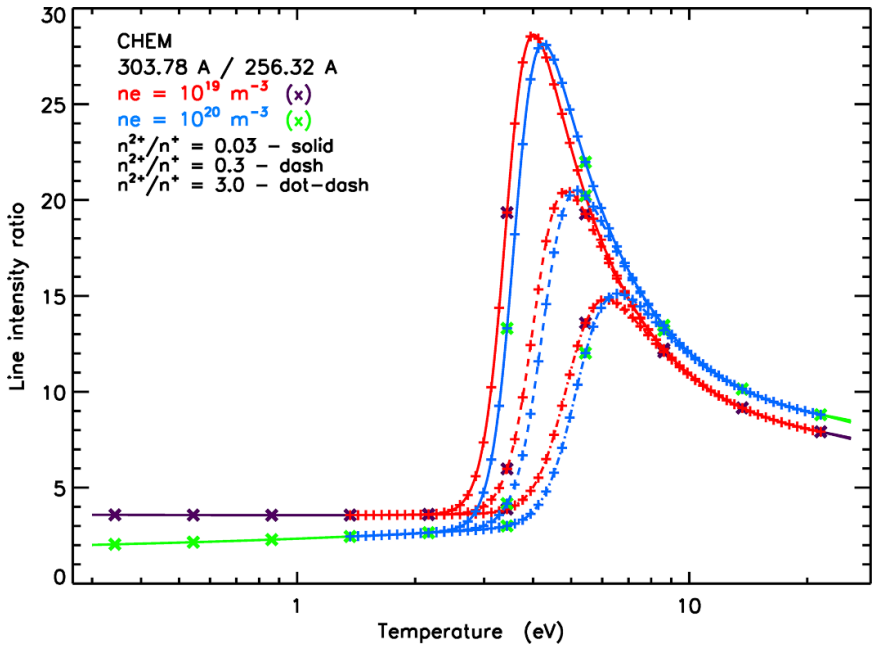

Figure 52. CHEM Lyman α to β line intensity ratios for two electron densities and three fully stripped He to He II ion density ratios. The data points from CHEM are shown, together with interpolated values.

Figure 50 shows the Lyman δ to Balmer γ line intensity ratio as a function of the latter's intensity, data being included from both operational periods. The high density limit of the 'branching ratio' is shown. The measurements fall $\sim$10% below the theory, which given the very low intensity of the Balmer γ observations and the complexity of calibrating the Lyman δ intensity, is regarded as being very satisfactory. More importantly, the Balmer γ line is not present in the spectrum without the Lyman δ line being clearly seen. From the analysis of both 'branching ratios' it is concluded that, even if the Lyman line intensities are affected by opacity, there is no evidence to suggest that their intensities cannot be reliably measured.

5. Discrepancies between JET measurements and theory

Discrepancies between JET observations and the theoretical CR models used to describe the hydrogen-like line intensities were first found for D and, subsequently, similar

Table 7. Results of minimization including and excluding the Lyman α/β ratio.

Parameter	Initial value (weight)	Upper and lower bounds (measurement)	Including α/β		Excluding α/β	
			CHEM	ADAS	CHEM	ADAS
T_e (eV)	4.0	0.2–25.0	4.01	4.25	4.41	4.95
$\mathrm{Log}_{10}(n_e)$ (m^{-3})	19.0	18.0–21.0	18.0	18.0	18.74	18.50
n^{2+}/n^{+} ratio	0.1	0.001–3.0	3.0	3.0	0.001	(0.3)[a]
α/β	(1.0)	(5.45)	6.14	5.85	27.9	23.6
β/γ	(1.0)	(3.57)	2.26	2.21	3.98	3.57
β/δ	(0.9)	(9.15)	3.64	3.85	8.47	9.15
β/ε	(0.8)	(31.2)	5.37	—	29.0	—
β/ζ	(0.7)	(68.4)	7.68	—	70.1	—
RMS fractional difference			0.56	0.39	0.075	0.001

[a] In the ADAS case in which the Lyman α to β ratio is excluded the n^{2+}/n^{+} ratio is fixed.

results were found for He II. As explained in section 3, an analysis of He II has advantages over that of D I and so the present illustration uses the He II measurements given in table 5. Comparisons are made with two CR models, ADAS (Summers 2004) and CHEM (Lawson *et al* 2019). The ADAS data are taken from the file 'home/adas/adas/adf15/pec96#he/pec96#he_pju#he1.dat', which includes photon emission coefficients for transitions up to the Lyman δ line. The CHEM data is available for all necessary transitions, although only for temperatures at which electron collisional excitation rate coefficients were calculated by Aggarwal *et al* (2017). It was necessary to interpolate the various atomic data used as described by Lawson *et al* (2023). Figures 51 and 52 show the ADAS and CHEM theoretical Lyman α to β line intensity ratios, respectively, for $n_e = 10^{19}$ and 10^{20} m^{-3} and three fully stripped to singly charged (n^{2+}/n^{+}) He ion density ratios. It can be seen that the data are similar. Additional ratios are illustrated by Lawson *et al* (2023).

For a stringent test of the CR models it is essential to compare line intensity ratios, since the relative sensitivity calibrations in the VUV spectral region are known more accurately than the absolute calibration. Indeed, the accuracy of the relative sensitivity calibrations of the JET spectrometers in the spectral range including the He Lyman series is better than $\pm 10\%$. The function

$$\sum_i w_i \left(\frac{R_{\mathrm{mod},i} - R_{\mathrm{meas},i}}{R_{\mathrm{meas},i}} \right)^2$$

was minimized using the IDL CONSTRAINED_MIN routine. $R_{\mathrm{mod},i}$ is the modelled line intensity ratio for the ith ratio, $R_{\mathrm{meas},i}$ the corresponding measured line intensity ratio and w_i a weighting to account for differences in measurement accuracies. The summation includes all ratios for which there are both measurements and atomic data. A function in which absolute fractional differences were used in the minimization instead of the square was also tested but gave very similar results.

Various minimizations were tried. The examples given in table 7 varied T_e, $\mathrm{Log}_{10}(n_e)$ and the n^{2+}/n^{+} ratio. Since it was not clear how sensitive the minimizations were to the n^{2+}/n^{+} ratio and $\mathrm{Log}_{10}(n_e)$, these parameters were sometimes fixed. For both the ADAS and CHEM CR models, the only cases found that gave a level of agreement approaching the measurement accuracy were those that excluded the Lyman α to β ratio from the minimization. In these cases, the measured Lyman α to β ratio was a factor of 4–5 lower than that predicted. This led to the consideration that opacity might routinely be affecting the Lyman intensities. By including a treatment of opacity in the CR model it was possible to explain the He II line intensity ratios (Lawson *et al* 2023). However, this treatment was found to be incompatible with certain D data. Since the same explanation was required for both D I and He II, the routine occurrence of opacity was rejected.

6. Conclusions

It is important to understand the behaviour of the hydrogen-like fuel species in tokamak plasmas. This is essential if reliable transport simulations of the plasma edge and divertor are to be carried out as well as being required in analyses of wall erosion, amongst others. However, poor agreement has been found between measurements of D and He Lyman series line intensities on JET and the well established theoretical models that describe these intensities. Consequently, measurements have been made of Lyman series line intensities and their ratios. In this paper results are presented for the He fuel, for which the analysis is simpler than for D. This is of value both in its own right, for example when He is used as a discharge fuel and to model the He ash produced during fusion reactions, and as a proxy for better understanding of the more complex D model and measurements.

Three operational periods have been studied, two in the C38 JET-ILW campaign and one in an earlier JET-C campaign. One feature found in this analysis is that the temperature dependent line intensity ratios usually have the same near-constant values, which would imply that the emission originates in plasma regions with the same electron temperature. Such behaviour is unexpected given the wide range of temperatures that are derived for the emission volumes of most impurity lines and divertor and edge particle transport simulations will be needed

to understand fully the marked differences between the fuel and impurity ions. All pulse surveys demonstrate that the near-constant line intensity ratios apply to the phases of a discharge during which the He intensities are comparatively low. This is the case for observations from all three periods studied, to those with a horizontal view into the bulk plasma, a view towards the outer divertor throat and to those directly viewing the divertor, the measured ratios being, within errors, the same for all cases studied. That the ratios do not depend on the line-of-sight would suggest localized regions of He II emission, since the view into the divertor encompasses very different plasma conditions than the one through the bulk plasma.

The all pulse surveys both illustrate the frequency with which pulses display the near-constant line intensity ratios and also allow exceptional pulses to be identified. In general, these have intense He emission, in a number of cases with significant additional heating. A dependence of the Lyman ratios on high Lyman α intensities is demonstrated. The time developments of the He II line intensities for a number of pulses are shown, including pulses in which the ratios are near-constant and those deviating from this behaviour. Observations from a poloidally scanning spectrometer that views the divertor from the top of the machine are also presented. Although the spatial profiles for the first three series members are recorded from consecutive discharges, they nevertheless show marked similarities across the divertor and have ratios similar to those found when the observations are made in a single discharge.

To ensure that the Lyman line intensities are not unduly affected by opacity, which in extreme cases could make the measurements unreliable, comparisons have been made with higher series members. In tokamak plasmas, the lower levels of the higher series transitions have low populations preventing any significant absorption taking place. It was possible to find two branching ratios, Lyman γ to Paschen α and Lyman δ to Balmer γ, for this comparison. Whenever a higher series line was observed, the corresponding Lyman series member was seen in the VUV spectrum. This suggests that the Lyman series line intensities can be reliably measured, even if affected by opacity.

A set of line intensity ratios measured at a particular Lyman α line intensity has been tabulated. This is regarded as the most reliable dataset for the near-constant line intensity ratios. The dataset has been used to illustrate the discrepancy between the observations and two current theoretical CR models. It will be of value for comparison with improved theoretical models which it is expected will lead to an understanding of the discrepancies between the models and measurements.

Data availability statement

All data that support the findings of this study are included within the article (and any supplementary files).

Acknowledgments

This work has been carried out within the framework of the EUROfusion Consortium, funded by the European Union via the Euratom Research and Training Programme (Grant Agreement No 101052200—EUROfusion) and from the RCUK Energy Programme [Grant Number EP/W006839/1]. The views and opinions expressed are however those of the authors only and do not necessarily reflect those of the European Union or the European Commission. Neither the European Union nor the European Commission can be held responsible for them.

ORCID iDs

K D Lawson https://orcid.org/0000-0002-1251-6392
M Groth https://orcid.org/0000-0001-7397-1586

References

Aggarwal K M, Igarashi A, Keenan F and Nakazaki S 2017 *Atoms* **5** 19
Arnaud M and Rothenflug R 1985 *Astron. Astrophys. Suppl. Ser.* **60** 425
Bonnin X, Dekeyser W, Pitts R, Coster D, Voskoboynikov S and Wiesen S 2016 *Plasma Fusion Res.* **11** 1403102
Borodkina I *et al* 2024 *Nucl. Fusion* **64** 106009
Conway N J, Cackett A J, Maggi C F, Meigs A G, Zastrow K-D, Biewer T M and Hillis D L 2018 *Rev. Sci. Instrum.* **89** 10K107
Fonck R J, Ramsey A T and Yelle R V 1982 *Appl. Opt.* **21** 2115
Groth M *et al*, 2023 *Proc. IAEA-FEC* (*London, UK*)
Huber A *et al* 2021 *Phys. Scr.* **96** 124046
Lawson K D *et al* 2012 *Rev. Sci. Instrum.* **83** 10D536
Lawson K D *et al* 2022 He II Lyman series line intensity measurements in the JET tokamak *JET Report*
Lawson K D *et al* 2023 Comparison between He II Lyman series line intensity measurements in the JET tokamak and collisional-radiative models *JET Report*
Lawson K D, Aggarwal K M, Coffey I H, Keenan F P and O'Mullane M G 2019 *J. Phys.* B **52** 045001
Lawson K D, Aggarwal K M, Coffey I H, Keenan F P, O'Mullane M G, Ryć L and Zacks J 2011 *Plasma Phys. Control. Fusion* **53** 015002
Lawson K D, Coffey I H, Zacks J and Stamp M F (JET-EFDA contributors) 2009 *J. Instrum.* **4** 04013
Lawson K D and Peacock N J 1988 *Opt. Commun.* **68** 121
Romazanov J *et al* 2024 *Nuc. Fusion* **64** 086016
Schwob J L, Wouters A W, Suckewer S and Finkenthal M 1987 *Rev. Sci. Instrum.* **58** 1601
Summers H P 2004 *The ADAS User Manual, version 2.6* (available at: https://open.adas.ac.uk)
Tonello E *et al* 2024 *Plasma Phys. Control. Fusion* **66** 065006
Verhaegh K *et al* 2021 *Nucl. Fusion* **61** 106014
Verhaegh K *et al* 2023 *Nucl. Fusion* **63** 016014
Wiesen S *et al* 2015 *J. Nucl. Mater.* **463** 480
Wolf R C *et al* 1995 JET Preprint, JET-P(95), 34